

國立交通大學

資訊科學與工程研究所

碩 士 論 文

利 用 導 場 向 量 空 間 投 影
進 行 腦 部 獨 立 活 動 訊 號 源 之 時 空 造 影



Lead Field Vector Space Projection for Spatiotemporal
Imaging of Independent Brain Activities

研 究 生：陳姿樺

指 導 教 授：陳永昇 博士

中 華 民 國 九 十 七 年 八 月



利用導場向量空間投影進行腦部獨立活動訊號源之時空造影
Lead Field Vector Space Projection for Spatiotemporal Imaging
of Independent Brain Activities

研究生：陳姿樺

Student : Tzu-Hua Chen

指導教授：陳永昇

Advisor : Yong-Sheng Chen

國立交通大學
資訊科學與工程研究所
碩士論文



Submitted to Institute of Computer Science and Engineering

College of Computer Science

National Chiao Tung University

in partial Fulfillment of the Requirements

for the Degree of

Master

in

Computer Science

August 2008

Hsinchu, Taiwan, Republic of China

中華民國九十七年八月



國立交通大學

研究所碩士班

論文口試委員會審定書

本校 資訊科學與工程 研究所 陳姿樺 君

所提論文：

Lead Field Vector Space Projection for Spatiotemporal
Imaging of Independent Brain Activities

利用導場向量空間投影進行腦部獨立活動訊號源之
時空造影

合於碩士資格水準、業經本委員會評審認可。

口試委員：蔡志鏗 陳永昇

孫賢修 陳醒吉

指導教授：陳永昇

所長：曾文忠

中華民國九十七年八月十九日



國立交通大學

博碩士論文全文電子檔著作權授權書

(提供授權人裝訂於紙本論文書名頁之次頁用)

本授權書所授權之學位論文，為本人於國立交通大學資訊科學與工程研究所 組，97 學年度第 一 學期取得碩士學位之論文。

論文題目：利用導場向量空間投影進行腦部獨立活動訊號源之時空造影
指導教授：陳永昇

■ 同意

本人茲將本著作，以非專屬、無償授權國立交通大學與台灣聯合大學系統圖書館：基於推動讀者間「資源共享、互惠合作」之理念，與回饋社會與學術研究之目的，國立交通大學及台灣聯合大學系統圖書館得不限地域、時間與次數，以紙本、光碟或數位化等各種方法收錄、重製與利用；於著作權法合理使用範圍內，讀者得進行線上檢索、閱覽、下載或列印。

論文全文上載網路公開之範圍及時間：

本校及台灣聯合大學系統區域網路	■ 中華民國 98 年 8 月 27 日公開
校外網際網路	■ 中華民國 98 年 8 月 27 日公開

■ 全文電子檔送交國家圖書館

授權人：陳姿樺

親筆簽名：

中華民國 97 年 08 月 28 日



國立交通大學

博碩士紙本論文著作權授權書

(提供授權人裝訂於全文電子檔授權書之次頁用)

本授權書所授權之學位論文，為本人於國立交通大學資訊科學與工程研究所 甲 組，97 學年度第 一 學期取得碩士學位之論文。

論文題目：利用導場向量空間投影進行腦部獨立活動訊號源之時空造影

指導教授：陳永昇

■ 同意

本人茲將本著作，以非專屬、無償授權國立交通大學，基於推動讀者間「資源共享、互惠合作」之理念，與回饋社會與學術研究之目的，國立交通大學圖書館得以紙本收錄、重製與利用；於著作權法合理使用範圍內，讀者得進行閱覽或列印。

本論文為本人向經濟部智慧局申請專利(未申請者本條款請不予理會)的附件之一，申請文號為：_____，請將論文延至____年____月____日再公開。

授權人：陳姿樺

親筆簽名：

陳姿樺

中華民國

97 年 08 月 28 日



國家圖書館 博碩士論文電子檔案上網授權書

(提供授權人裝訂於紙本論文本校授權書之後)

ID:GT00955531

本授權書所授權之論文為授權人在國立交通大學資訊科學與工程研究所 97 學年度第一學期取得碩士學位之論文。

論文題目：利用導場向量空間投影進行腦部獨立活動訊號源之時空造影

指導教授：陳永昇

茲同意將授權人擁有著作權之上列論文全文(含摘要)，非專屬、無償授權國家圖書館，不限地域、時間與次數，以微縮、光碟或其他各種數位化方式將上列論文重製，並得將數位化之上列論文及論文電子檔以上載網路方式，提供讀者基於個人非營利性質之線上檢索、閱覽、下載或列印。

※ 讀者基於非營利性質之線上檢索、閱覽、下載或列印上列論文，應依著作權法相關規定辦理。

授權人：陳姿樺

親筆簽名：

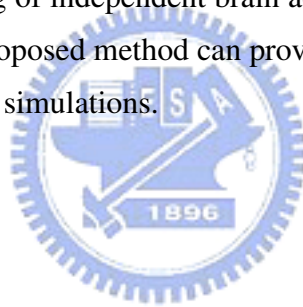


民國 97 年 08 月 08 日



Abstract

Magnetoencephalography (MEG) and Electroencephalography (EEG) are the non-invasive instruments that record the induced magnetic field and scalp electrical potential. To study the functionality of human brain, inverse algorithms, involves forward model in lead field vector space, are commonly used for estimating cortical source distribution. For more precisely estimation, interferes, such as artifacts and environmental noises, must be removed. Independent Component Analysis (ICA) can be used to remove interferes which are assumed to be independent to brain activities. Moreover, ICA also provides the scalp topography, or said the mixing matrix, of components. The proposed method aim to find the cortical source distribution of given independent components by find a set of basis that best represents the mixing matrix using Singular Value Decomposition (SVD). It provides the spatiotemporal imaging of independent brain activities that cannot obtain from ICA. It is demonstrated that the proposed method can provide accurate cortical source distribution from experiment results of simulations.



摘要

腦磁圖儀(Magnetoencephalography)及腦電圖儀(Electroencephalography)利用非侵入式感測器量測因腦部神經元活化所產生的磁場及電位差。為了解腦部協調及控制行為的機制一般均以逆估算演算法(inverse algorithm)分析感測器所量測的訊號以得知大腦皮質層的活動動態。逆估算演算法可建立於導場向量空間(lead field vector space)模型的假設上且利用條件限制以求得大腦皮質層活動動態分佈。為更精準求得大腦皮質層活動動態分佈，必須去除人體內在或外在雜訊對腦部活動訊號的干擾。若假設腦部活動訊號與雜訊互相獨立，則獨立成分分析(Independent Component Analysis)可運用於分離腦部活動訊號及其干擾源。此外，獨立成分分析亦可求得獨立訊號對應之感測器空間(sensor space)活動動態。此論文利用奇異值分解(Singular Value Decomposition)導場矩陣(lead field matrix)得到一組最足以代表在感測器空間中獨立時序訊號之動態分佈(mixing matrix)的基底(basis)並運用獨立成分分析產生在感測器空間中獨立時序訊號之動態分佈以求得大腦皮質層活動動態。此研究突破獨立成分分析演算法不具有時空造影之限制，且模擬實驗驗證此方法可精確得到獨立活動訊號在大腦皮質層活動動態分佈。



Contents

List of Figures	v
List of Tables	vii
1 Introduction	1
1.1 Backgrounds	2
1.2 Thesis Scope	3
1.3 Thesis Organization	4
2 Related Works	5
2.1 MEG/EEG Forward Model with Spherical Head Model	7
2.2 Inverse Solution	9
2.3 Independent Component Analysis (ICA)	12
2.4 Electromagnetic Spatiotemporal Independent Component Analysis (EM-SICA)	13
2.5 Comparison between ICA and EMSICA	15
3 Spatiotemporal Imaging of Independent Brain Activities	17
3.1 Mixing Matrix Approach for Imaging Method	18
3.2 Unmixing Matrix Approach for Imaging Method	19
4 Experiments	21
4.1 Materials	22
4.1.1 3D MR Images	22
4.1.2 Cortical Surface Reconstruction	23
4.1.3 MEG Device	24
4.1.4 Data Preprocessing	25
4.2 Experiments	25
4.2.1 Simulation 1 - A Single Sine Dipolar Source	26
4.2.2 Simulation 2 - Two Uncorrelated Dipolar Sources	32
4.2.3 Simulation 3 - Four Sine Dipolar Sources	37
4.2.4 Experiments of Gender Discrimination	45

5 Discussion and Conclusions	59
5.1 Discussion	60
5.1.1 Accuracy and Capabilities	60
5.1.2 Cortical Surface Constraints	60
5.1.3 Estimation With Less Parameters	61
5.1.4 Limitations	62
5.2 Conclusions	63
5.3 Future Works	64
Bibliography	65



List of Figures

2.1	MEG/EEG Forward Model	8
2.2	Independent Component Analysis	12
2.3	EMSICA	14
2.4	Infomax ICA in sensor space vs. EMSICA on cortical surface	15
3.1	Work flow - lead field vector space projection for spatiotemporal imaging of Independent Brain Activities	20
4.1	Surface of Brain	23
4.2	Reconstructed Pia Mater	24
4.3	Simulation 1 - The Output Measurement and Topography on 250 ms	27
4.4	Simulation 1 - Ground Truth	27
4.5	Simulation 1 - ICA Decomposition	29
4.6	Simulation 1 - the reconstructed measurement and topography	29
4.7	Simulation 1 - Cortical Source Distribution Using Unmixing Matrix Approach	30
4.8	Simulation 1 - Cortical Source Distribution Using Mixing Matrix Approach	31
4.9	Simulation 2 - The Output Measurement and Topography	32
4.10	Simulation 2 - Ground Truth	33
4.11	Simulation 2 - ICA Decomposition	34
4.12	Simulation 2 - Cortical Distribution	35
4.13	Simulation 2 - Cortical Distribution	36
4.14	Simulation 3 - The Output Measurement and Topography	38
4.15	Simulation 3 - Ground Truth	39
4.16	Simulation 3 - the reconstructed measurement and topography	39
4.17	Simulation 3 - ICA Decomposition	40
4.18	Simulation 3 - Leakage of the 2nd Component	40
4.19	Simulation 3 - Cortical Distribution	42
4.20	Simulation 3 - Cortical Distribution	43
4.21	Simulation 3 - Cortical Distribution	44
4.22	Experiment Paradigm of Gender Discrimination	46

4.23 ICA Result of Real Data	47
4.24 Preprocessed Measurements and Cortical Source Distribution Calculated by MCB of Real Data	49
4.25 Cortical Source Distribution of Real Data - Group 1	50
4.26 Cortical Source Distribution of Real Data - Group 2	50
4.27 Cortical Source Distribution of Real Data - Group 3	51
4.28 Cortical Source Distribution of Real Data - Group 4	51
4.29 Cortical Source Distribution of Real Data - Group 5	52
4.30 Cortical Source Distribution of Real Data - Group 6	53
4.31 Cortical Source Distribution of Real Data - Group 7	54
4.32 Cortical Source Distribution of Real Data - Group 8-1	55
4.33 Cortical Source Distribution of Real Data - Group 8-2	56
4.34 Cortical Source Distribution of Real Data - Group 8-3	57
5.1 Lead Fields of Given Source and Peak of Cortical Source Distribution of Simulation 1	61
5.2 Two Lead Fields Vectors Calculated by MCB Using Real Data	62



List of Tables

4.1	Simulation 1 - Location Error and Similarity	28
4.2	Simulation 2 - Ground Truth	32
4.3	Simulation 2 - Location Error and Similarity	34
4.4	Simulation 3 - Ground Truth	37
4.5	Simulation 3 - Location Error of Cortical Source Distribution	41





Chapter 1

Introduction



1.1 Backgrounds

For the past thousands of years, people had dedicated themselves to study the functionality of human brain since it plays an important role in coordinating all parts of the body. The researches were limited in technical skill and morality that it was not allowed to do invasive anatomical experiments on living bodies. Recently, more and more non-invasive instruments have been invented, such as Magnetoencephalography (MEG), Electroencephalography (EEG), functional Magnetic Resonance Imaging (fMRI) and Near Infrared Reflectance Spectroscopy (NIRS), because of the thriving development of technology. Thus, it provides solutions for studying brain activities without physical harm. According to the neurophysiological knowledge, activation of neurons in brain causes changes in blood flow and oxygen levels and thus can be regarded as neural activity. fMRI and NIRS are the instruments for detecting hemodynamic and hemoglobin changes with high spatial resolution up-to 1 mm and 800 nm but with low temporal resolution resulted from the slow hemodynamic changes in seconds. In contrast, MEG and EEG are two instruments that measure induced magnetic field and scalp electric potential produced by ion flow and thus have the higher temporal resolution in milliseconds than fMRI has.

Because the brain activities may dynamically change up-to-80 Hz and in accordance with Nyquist sampling theorem [27], temporal resolution with at least 160 Hz sampling frequency is required to reconstruct the original signals. Therefore, MEG and EEG are more suitable for studying neural dynamics. In studying of brain functionality by recording of MEG and EEG, the two major difficulties are the ill-posed inverse problem and low Signal-Noise-Ratio (SNR). First, the forward model, including the lead field vector representing distribution of brain activities to sensor array, is involved in the inverse problem in order to reconstruct brain activity and is going to be introduced in Section 2.2.

For low SNR, it results from the much smaller scale of electrophysiological signal than of environmental noises. For instance, the magnitude of omnipresent static field of earth is around 10^{-1} Tesla and is much larger than of the induced magnetic field which is around 10^{-10} to 10^{-15} Tesla. In addition, MEG and EEG signals are often corrupted with the background brain activities and artifacts, such as the heartbeat, eye-blink, and environmental noises. Thus, data preprocessing, including bandpass filter and baseline correction, and

Independent Component Analysis (ICA) are some commonly adopted techniques for increasing the SNR or rejecting artifacts. ICA was originally proposed for the purpose of blind source separation to find components that are mutually statistical independent [21]. It performs best when raw or unaveraged signals are applied as inputs. Recently, it has been proved a useful tool in neurological brain research and is widely-used for analyzing MEG/EEG signals [18, 19], especially for removing artifacts based on its independence assumption [4, 8, 17, 22]. Moreover, it may be probable to see the event-related fields (ERFs) after removing noises. However, ICA has limitations that the number of independent components is less than or equal to the number of sensors and it provides the sensor space distribution of components but no cortical distribution. It is insufficient for studying brain activities. The more details of ICA will be described in Section 2.3.

Electromagnetic Spatiotemporal Independent Component Analysis (EMSICA) was proposed by Arthur C. Tsai et al. in 2006 [33] for estimating spatiotemporal independent EEG components and the corresponding cortical source distribution simultaneously. It is implemented using Bayesian statistical framework for imaging independent brain activities under physiological source constraints. Hence, the max number of the output components becomes tens of thousands since cortical source location and orientation are used for estimation. On the other hand, the number of unknown parameters of EMSICA is much more than of standard ICA and then it becomes harder to be solved.

We propose a new method to directly map independent components extracted by standard ICA to cortical surface by projection of lead field vector space. It provides an both intuitive and efficient solution for studying interested components or the discovered features further.

1.2 Thesis Scope

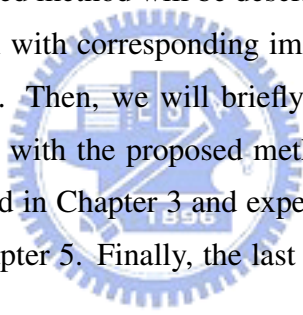
In this thesis, we focus on the imaging method for solving cortical source distribution of independent components extracted using the standard ICA algorithms. It is neither for solving the inverse problem nor for more precisely decomposing independent component, but it can be helpful and provides a both intuitive and efficient solution for mapping the

discovered features or interested components of MEG/EEG signals to cortical surface. According to the experiments result demonstrated in Chapter 4, it shows the high accuracy and capability of our imaging method.

In this work, cortical surface were reconstructed by FreeSurfer , a set of software tools for study of cortical and subcortical anatomy and VTK, a visualization toolkit and open source software for 3D computer graphics. We implemented the proposed method using C++ and matlab. The program for visualization of 3D cortical surface and source distribution were implemented using Java. All these program were executed on Win32 platform except that FreeSurfer was executed on Linux x86_64 platform.

1.3 Thesis Organization

In the later Chapter, the proposed method will be described in detail. First, background knowledge such as forward model with corresponding imaging methods and ICA will be introduced in Section 2.2 and 2.3. Then, we will briefly describe EMSICA, the related work, in Section 2.4 and compare with the proposed method in Chapter 5. Detail of the proposed method will be illustrated in Chapter 3 and experiments result will be displayed in Chapter 4 and discussed in Chapter 5. Finally, the last two section will be conclusions and future works.



Chapter 2

Related Works



MEG and EEG detect the induced magnetic field and scalp electrical potential outside of head. In studying of brain functionality by recording of MEG and EEG, the two major difficulties are the ill-posed inverse problem and low Signal-Noise-Ratio (SNR).

First, the forward model, including the lead field vector representing distribution of brain activities to sensor array, is involved in the inverse problem in order to reconstruct brain activities. Therefore, based on the forward model, several groups of methods were proposed to solve the inverse problem or to map sources to cortical surface. An inverse algorithm aims for estimation of real source location and orientation, such as dipole fitting. An imaging method tries to estimate the statistical map of MEG/EEG signals that indicates the cortical source distribution in probability. The higher probability it is, the more possible stronger activation it has. Otherwise, according to the approach of imaging method or inverse algorithm, it can be separated into two categories such as scanning approach and imaging approach.

For low SNR, it results from the much smaller scale of electrophysiological signal than of environmental noises. In addition, MEG and EEG signals are often corrupted with the background brain activities and artifacts, such as the heartbeat, eye-blink, and environmental noises. Thus, data preprocessing, including bandpass filter and baseline correction, and Independent Component Analysis (ICA) are some widely used techniques for increasing the SNR or rejecting artifacts.

ICA was originally proposed for the purpose of blind source separation to find components that are mutually statistical independent [21]. Recently, it has been proved a useful tool in neurological brain research and is widely-used for analyzing MEG/EEG signals [18, 19], especially for removing artifacts or finding features based on its independence assumption [4, 8, 17, 22]. Moreover, it may be probable to see the event-related fields (ERFs) after removing noises. However, ICA has limitations that the number of independent components is less than or equal to the number of sensors and it provides the sensor space distribution of components but no cortical distribution. It is insufficient for studying brain activities.

Electromagnetic Spatiotemporal Independent Component Analysis (EMSICA) was proposed by Arthur C. Tsai et al. in 2006 [33] for estimating spatiotemporal independent EEG components and the corresponding cortical source distribution simultaneously. Thus, it

has the same ability of mapping sources to cortical surface as imaging methods for solving inverse problem. It also has the same ability of separating independent components as ICA.

However, it may be harder to have a best solution for EMSICA than for standard ICA since EMSICA has much more unknown parameters that results from the cortical surface constraints.

We propose an imaging method for mapping independent components to cortical surface with less unknown parameters by standard ICA. But it can achieve the same work like EMSICA.

2.1 MEG/EEG Forward Model with Spherical Head Model

Inverse algorithms have to involve forward solution for estimating the properties of brain sources when given a set of MEG/EEG signals measured by an array of external sensors. Therefore, the forward model, describes the distribution of magnetic field outside of head when given a theoretical brain source, should be constructed at first.

The most commonly adopted head model, the spherical model, assumes that it is comprised by a set of nested concentric sphere shells representing brain, skull and scalp [2, 25]. Each sphere has homogeneous and isotropic conductivity. Under this assumption, consider the simple case of a unit current dipole with the parameter $\theta = \{\mathbf{r}, \mathbf{q}\}$, located at $\mathbf{r} \in \mathbb{R}^3$ with orientation $\mathbf{q} \in \mathbb{R}^3$. The lead field vector $\mathbf{l}_\theta \in \mathbb{R}^N$, a column vector, indicates how this current dipole distributes to the MEG sensor array and can be illustrated as a single topography like Figure 2.1.

$$\mathbf{l}_\theta = \mathbf{G}_\mathbf{r} * \mathbf{q} \quad (2.1)$$

The gain matrix $\mathbf{G} \in \mathbb{R}^{N*3}$ describes the sensibility of N MEG/EEG sensors to the current dipole in the three dimensional Cartesian coordinate system.

Furthermore, concentrate on the general case in volume domain, the MEG/EEG measurement $\mathbf{m}(t) \in \mathbb{R}^N$ recorded at time t is composed of many time-varying current densi-

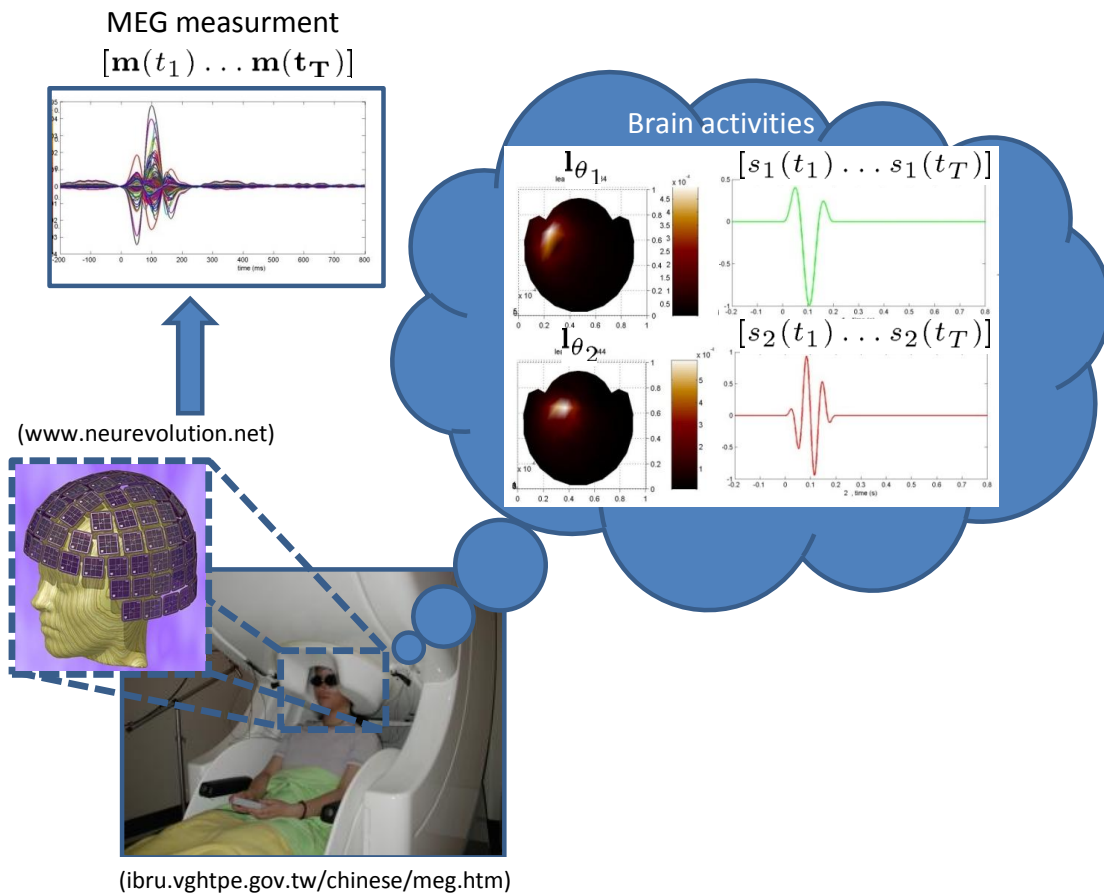


Figure 2.1: **MEG Forward Model.**

(The picture of MEG is excerpted from <http://ibru.vghtpe.gov.tw/chinese/meg.htm>.)

(The picture of sensor is excerpted from <http://www.neurevolution.net>.)

While an oriented current dipole generated by an activated neuron, the MEG instrument acquires induced magnetic field by sensor array and output the time course, or measurement. Each lead field vector with respect to a current dipole can be regarded as a topography or source distribution to MEG sensors.

ties with their respective lead field vector illustrated by the following equation

$$\mathbf{m}(t) = \sum_{\forall i} \mathbf{l}_{\theta_i} * s_i(t) + \mathbf{n}(t) = [\mathbf{l}_{\theta_1} \mathbf{l}_{\theta_2} \dots] \begin{bmatrix} s_1(t) \\ s_2(t) \\ \vdots \end{bmatrix} + \mathbf{n}(t) \quad (2.2)$$

where $\mathbf{n}(t)$ is the additive noise. Let $\mathbf{L} = [\mathbf{l}_{\theta_1} \mathbf{l}_{\theta_2} \dots]$ denotes the lead field matrix and $\mathbf{s}(t) = [s_1(t) s_2(t) \dots]^T$ denotes the time-varying current densities. Then, the equation can be rewritten as

$$\mathbf{m}(t) = \mathbf{L}\mathbf{s}(t) + \mathbf{n}(t). \quad (2.3)$$

Figure 2.1 can be used for explaining the forward model. While a neuron is activated, the induced magnetic field or scalp electric potential is detected by sensors of MEG or EEG. The topography represents the distribution of the magnetic field or electric potential produced by a unit dipole and is so called a lead field vector. Unit dipole with different location and orientation will result in different lead field vector. Thus, linear combined sources with the respective lead field vectors and amplitude plus the additive noises are included in measurement.

2.2 Inverse Solution

The inverse problem is an ill-posed problem of determining the neuronal sources from MEG/EEG measurement and has no unique solution. Thus, it is impossible to specify distribution of neuronal sources without any further assumptions or anatomical constraints. According to the revealed MEG/EEG researchs, parametric and imaging methods are the two general approaches for estimating neuronal sources [2, 26].

Parametric or Scanning Methods

The parametric or scanning methods solving the inverse problem under the assumption that sources can be represented by a few equivalent current dipoles (ECDs) of unknown locations, orientations and amplitude to be estimated with nonlinear numerical method [2, 13, 16, 26]. Thus, a current dipole is assigned to each tessellation elements,

numbering in tens of thousands, on the cortical surface orientated to the radial line, or said the local surface normal, during a period and trying to find the best fit of the MEG/EEG measurements.

The most common model used for inverse solution is the least-squares source estimation (Equation 2.4) [2, 7, 11]. It is a brute force approach, but with expensive resource and time cost, of nonlinear search by scanning through all possible set of locations, orientations and amplitude. It attempts to determine the set $\{\theta_i, s_i(t)\} = \{\{\mathbf{r}_i, \mathbf{q}_i\}, s_i(t)\}$ for $i = 1 \dots P$ that minimizes the square error between recording and the field computed from estimated sources $\tilde{\mathbf{s}}(t)$ using forward model $\tilde{\mathbf{L}}$ (Equation 2.3).

$$\arg \min \|\mathbf{m}(t) - \tilde{\mathbf{L}}\tilde{\mathbf{s}}(t)\| \quad (2.4)$$

Recently, beamforming approaches, performing spatial filter \mathbf{W} on data $\mathbf{m}(t)$ (Eq. 2.5), are applied in estimating cortical distribution of neuronal sources over least-squares with extra constraints [31,32], such as minimum norm (MNE) [12,15,20,23], minimum variance (LCMV and SAM) [28–30, 34] and maximum contrast (MCB) [5] constraints. [7].

$$\mathbf{s}(t) = \mathbf{W}^T \mathbf{m}(t) \quad (2.5)$$

However, these methods may result in spatial over-smoothing that does not explicitly express anatomical or physiological constraints in the source reconstruction process. It may comprehensively yield unrealistic solution. Moreover, one of the limitations of beamforming is that coherent sources with the true signal from the scanning location can cause cancellation of the interested signal. Not allowing source estimation throughout the entire event period is another one, thus leaving parts of the event unexplained.

Imaging Approaches

The imaging approaches estimate amplitudes of a set of dipoles with fixed locations within the brain volume. Similar to scanning method mentioned in last section, computing on the volumetric grid is the basic technique for imaging methods. Moreover, since the brain activities are believed to be restricted to the cortex and MEG is most sensitive to cortical sources, the imaging method can be constrained to the cortical surface that extracted

from an anatomical MR image of the subject. As aforementioned, sources can be placed on each point that forms the triangle mesh with orientation that perpendicular to the surface. Hence, the inverse problem is simplified to estimate linear parameters only. [6].

Bayesian statistic framework is a widely-used approximation of imaging method [1,2] such as FOCUSS [10,24].

$$p(\mathbf{S}|\mathbf{M}) = \frac{p(\mathbf{M}|\mathbf{S})p(\mathbf{S})}{p(\mathbf{M})} \quad (2.6)$$

$p(\mathbf{S}|\mathbf{M})$ denotes the conditional probability of an event \mathbf{S} assuming \mathbf{M} has occurred. That is, applying to the inverse problem, the conditional probability of sources \mathbf{S} activated assuming MEG/EEG measurement \mathbf{M} has been recored. In contrast, $p(\mathbf{M}|\mathbf{S})$ describes the forward problem that the conditional probability of the measurement \mathbf{M} been recorded assuming \mathbf{S} has activated and $p(\mathbf{S})$ is the prior. Therefore, the sources are estimated by maximization of the posterior probability.

$$\tilde{\mathbf{S}} = \arg \max p(\mathbf{M}|\mathbf{S})p(\mathbf{S}) \quad (2.7)$$

However, it has been revealed by Hillebrand et al. [14] that small errors in anatomical constraints can incur the large errors in source estimation. Moreover, the higher spatial resolution it is, the worse effects of errors it has. This may remove or decrease the advantage of estimating sources using imaging approaches and anatomical constraints.

2.3 Independent Component Analysis (ICA)

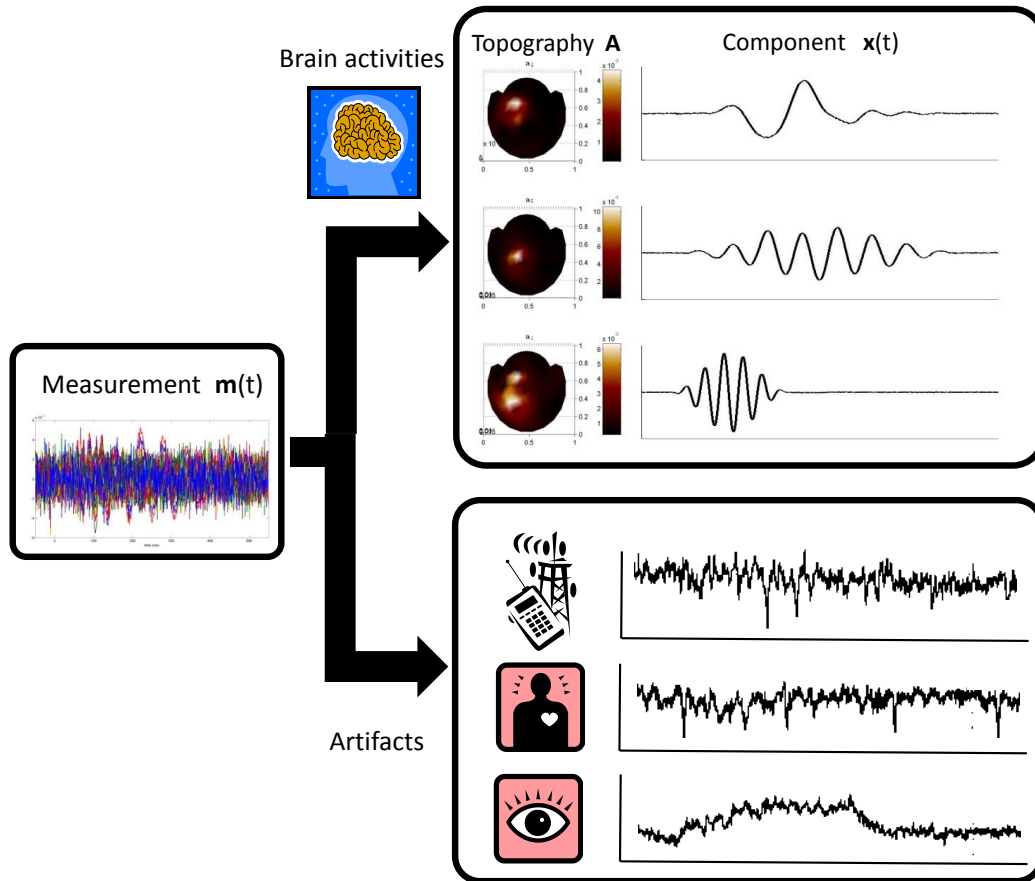


Figure 2.2: **Independent Component Analysis.** MEG/EEG signals are often corrupted by additive noises including background brain activities, heartbeat, eye-blinking, other electrical muscle activities and the environment noises. In general, these interferences occur independently to the stimuli or ERFs. Recently, ICA has been proved a useful tool in analyzing MEG/EEG signals, especially for artifacts removal. It attempts to find the unmixing matrix W that makes the output components as independent as possible.

MEG/EEG signals are often corrupted by additive noises including background brain activities, heartbeat, eye-blinking, other electrical muscle activities and the environment noises (Figure 2.2). In general, these interferences occur independently to the stimuli or event-related fields (ERFs).

Independent component analysis (ICA) was originally proposed for the purpose of

blind source separation to find components that are mutually statistical independent [21]. It performs best when raw or unaveraged signals are applied as inputs. Recently, it has been proved a useful tool in neurological brain research and is widely-used for analyzing MEG/EEG signals [18, 19], especially for removing the interferences mentioned above as a preprocessing step based on its independence assumption [4, 8, 17, 22]. Moreover, it may be probable to see the ERFs after removing noises and be helpful for the following source estimation process.

The ICA task is casted as follows:

$$\mathbf{m}(t) = \mathbf{A}\mathbf{x}(t) \quad (2.8)$$

, $\mathbf{A} \in \mathbb{R}^{N \times K}$ is so called a mixing matrix that compounds the K independent components $\mathbf{x}(t) \in \mathbb{R}^K$ into MEG measurement $\mathbf{m}(t)$. Each single column vector \mathbf{a}_i of mixing matrix \mathbf{A} is respected to the i^{th} component $\mathbf{x}_i = [x_i(t_1) \dots x_i(t_T)]$, for $i = 1 \dots K$, which specifies its distribution to MEG sensors. In contrast, the equation 2.8 can also be written as

$$\mathbf{W}^T \mathbf{m}(t) = \mathbf{x}(t) \quad (2.9)$$

where $\mathbf{W} \in \mathbb{R}^{N \times K}$ is the unmixing matrix. Each single column vector \mathbf{w}_i of unmixing matrix \mathbf{W} is a filter extracting the corresponding component \mathbf{x}_i from MEG measurement.

However, the amount of output independent components is limited to the number of input channels. That is, at most N components will be outputted if we send a N -channel MEG measurement to ICA.

2.4 Electromagnetic Spatiotemporal Independent Component Analysis (EMSICA)

Electromagnetic Spatiotemporal Independent Component Analysis (EMSICA) was proposed by Arthur C. Tsai et al. in 2006 [33] for estimating spatiotemporal independent EEG components and the corresponding cortical source distribution. It is implemented using Bayesian statistical framework for imaging independent brain activities under physiological source constraints.

First, it assumes that P brain activities are consisted of the K spatiotemporal independent components and the matrix $\mathbf{B} \in \mathbb{P} * \mathbb{K}$ describes the linear combination.

$$\mathbf{s}(t) = \mathbf{B}\mathbf{x}(t) \quad (2.10)$$

Each column vector \mathbf{b}_i , where $\mathbf{B} = [\mathbf{b}_1 \dots \mathbf{b}_K]$, represents the cortical distribution of component $x_i(t)$ for $i = 1 \dots P$. Thus, the forward solution (Eq. 2.3) becomes

$$\mathbf{m}(t) = \mathbf{L}\mathbf{s}(t) = \mathbf{L}\mathbf{B}\mathbf{x}(t). \quad (2.11)$$

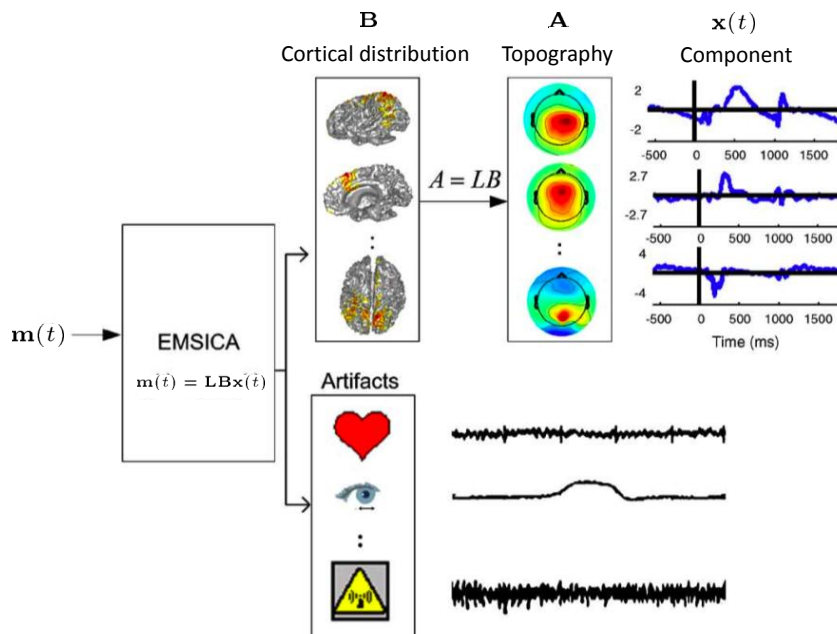


Figure 2.3: EMSICA.

(This picture is excerpted from [33])

EMSICA attempts to estimate the cortical distribution \mathbf{B} that makes the corresponding output components as independent as possible. Moreover, compare equation 2.8 for ICA and 2.11, distribution of independent components to sensors are obtained by Equation 2.12. Thus, there are distributions to both cortical surface and sensor space.

Similar to ICA, EMSICA attempts to estimate the cortical distribution \mathbf{B} that makes

the corresponding output components as independent as possible and K , the amount of components, must be less than or equal to P or said the number of brain activities.

2.5 Comparison between ICA and EMSICA

EMSICA and ICA both attempt to extract independent components from input signals and to find the respected distribution. According to the Equation 2.8 from ICA and 2.11 from EMSICA, the relation between distribution to sensor space from ICA and to cortical surface from EMSICA can be illustrated by

$$\mathbf{A} = \mathbf{L}\mathbf{B}. \quad (2.12)$$

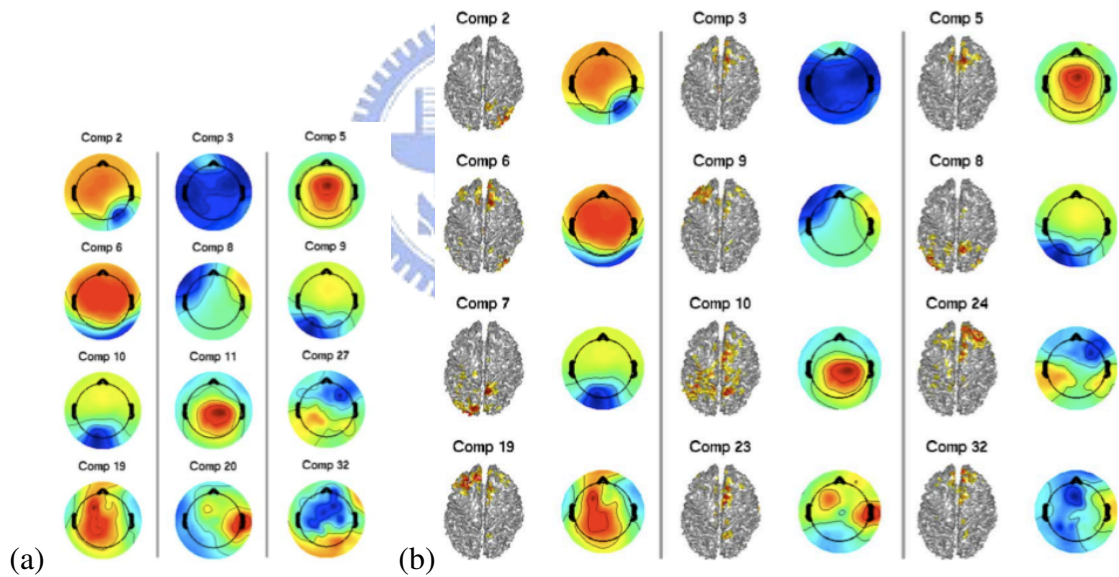


Figure 2.4: **Infomax ICA in sensor space vs. EMSICA on cortical surface.**

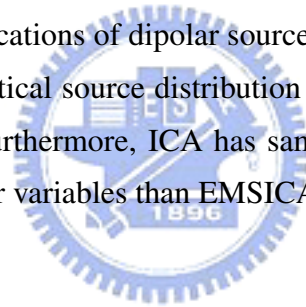
(These two pictures are excerpted from [33])

(a) Topography with respect to 12 components, accounting for sensorimotor mu, frontal midline theta, central and lateral posterior alpha rhythms, separated using infomax ICA.
 (b) Cortical distribution of the 12 components extracted by EMSICA and the corresponding topography by applying lead field matrix to cortical distribution map. Results of EMSICA similar to the ones of ICA demonstrates that EMSICA has the convinced ability to separate components well like what the widely-used ICA has.

Figure 2.4 displays the results of a two-back visual memory working memory task analyzing by standard ICA and EMSICA. The topographies, outputted by ICA, displayed in left-panel and the ones, transformed from cortical distribution by lead field matrix, displayed in right-panel are similar. This demonstrates that EMSICA has the convinced ability to separate components well like what the widely-used ICA has.

Moreover, EMSICA, within a single procedure, solves not only independent components but also the imaging of cortical source distribution by involving the forward solution and implemented using Bayesian framework. This makes the difference between ICA who is not an imaging method and just separates components in the same space as input signals. On the other hand, ICA can split components in cortical space as the second procedure but an imaging or inverse method to measurement required at first [35].

Comparing these two algorithms, EMSICA has the ability to estimate cortical source distribution but also has too many variables, at least 110,000 triangular points consisted of the cortical surface in our case, locations of dipolar sources need to be solved. In contrast, standard ICA cannot estimate cortical source distribution directly when applied measurement but not cortical sources. Furthermore, ICA has same accuracy in sensor space but handles the smaller data and fewer variables than EMSICA does.



Chapter 3

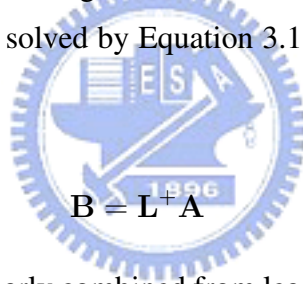
Spatiotemporal Imaging of Independent Brain Activities



Under the assumption, described in Section 2.4 by the forward solution (Equation. 2.11), brain activities $s(t)$ are composed of numbers of spatiotemporal independent components $x(t)$ with cortical distribution \mathbf{B} . We propose a method for spatiotemporal imaging of independent components, estimated using standard ICA, by lead field vector space projection. Thus, it has advantages of small data size and fewer variables like standard ICA but also has the ability to map independent components to cortical surface like EMSICA.

3.1 Mixing Matrix Approach for Imaging Method

According to equation 2.12, each mixing vector \mathbf{a}_i has its corresponding cortical distribution \mathbf{b}_i . They can be explained to the distribution of a component to sensors and cortical surface. Moreover, \mathbf{b}_i represents the linear combination of lead field vector that consists the respective mixing vector. Thus, if mixing matrix \mathbf{A} and lead field matrix \mathbf{L} are given, the cortical source distribution can be solved by Equation 3.1 where \mathbf{L}^+ is solved by singular value decomposition.



$$\mathbf{B} = \mathbf{L}^+ \mathbf{A} \quad (3.1)$$

Since mixing matrix \mathbf{A} are linearly combined from lead field matrix \mathbf{L} by the combination \mathbf{B} , we apply SVD to \mathbf{L} for finding a set of basis that well-represent the mixing matrix \mathbf{A} . Therefore, the linear combination \mathbf{B} is solvable when \mathbf{L}^+ and \mathbf{A} are known.

However, according to the definition of ICA, unmixing matrix \mathbf{W} is estimated at first for making the output components as independent as possible. Mixing matrix is calculated by Equation 3.2 from unmixing matrix \mathbf{W} for representing the distribution of components to sensors. Because \mathbf{A} is not real inverse of \mathbf{W} , there must exist some distortion of \mathbf{A} .

$$\mathbf{A} = \mathbf{W}^+ \quad (3.2)$$

Then, Equation 3.3 becomes Equation 3.3 but it remains in doubt. Both \mathbf{L}^+ and \mathbf{A}^+ are distorted. There must be too much distortion of the output \mathbf{B} . The effect were observed by simulation described in later chapter.

$$\mathbf{B} = \mathbf{L}^+ \mathbf{W}^+. \quad (3.3)$$

Consider the definition of ICA, \mathbf{W} seems more suitable for calculating the cortical source distribution and it is describe in next section.

3.2 Unmixing Matrix Approach for Imaging Method

The deduction starts from the forward equation 2.11 and assumes independent components spanning the whole signal space. By applying standard ICA to measurement to obtain the spatial filter or unmixing matrix \mathbf{W} , the corresponding outputs $\mathbf{x}(t)$, representing the time course of independent components at time t , can be illustrated by equation 3.4.

$$\mathbf{W}^T \mathbf{m}(t) = \mathbf{W}^T \mathbf{L} \mathbf{B} \mathbf{x}(t) = \mathbf{x}(t) \quad (3.4)$$

Moreover, the column vector $\mathbf{x}(t)$ is an eigenvector of matrix \mathbf{C} if we let $\mathbf{C} = \mathbf{W}^T \mathbf{L} \mathbf{B}$ and then $\mathbf{C} \mathbf{x}(t) = \mathbf{x}(t)$. Based on the assumption that independent components $\mathbf{x}(t)$ span the whole signal space, \mathbf{C} must be an identity matrix such that $\mathbf{W}^T \mathbf{L} \mathbf{B}$ is identity. Thus, the cortical source distribution \mathbf{B} can be solved by singular value decomposition (SVD) (Eq. 3.5).

$$\mathbf{B} = (\mathbf{W} \mathbf{L})^+ \quad (3.5)$$

In summary, Figure 3.1 illustrates the work flow of the proposed method. Standard ICA is applied as a preprocessing procedure for picking features and removing uninterested brain activities or other interferes. And then, project the interested components by lead field to obtain the corresponding cortical source distribution.

Work Flow

Figure 3.1 shows the work flow for spatiotemporal imaging of independent components. ICA is executed twice here. The first-stage ICA is for feature selection, or said reject the uninterested components and is regarded as a preprocess step. Thus, measurement should

be reconstructed using Equation 2.8 whenever the rejection is done. And then, second-stage ICA is executed for separating independent components for imaging in later steps.

Moreover, the lead field is made up under physiological source constraints, that is location and orientation is segmented from the MR image. Thus, it can be pre-cauculated for each subject.

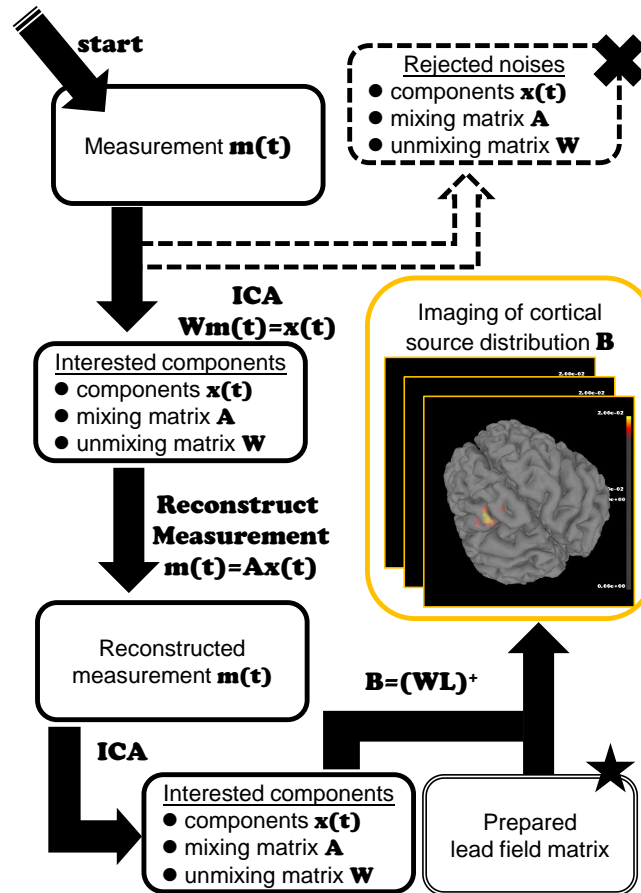


Figure 3.1: **Work flow - lead field vector space projection for spatiotemporal imaging of Independent Brain Activities** Standard ICA is applied as a preprocessing procedure for picking features and removing uninterested brain activities or other interferences. And then, project the interested components by lead field to obtain the corresponding cortical source distribution.

Chapter 4

Experiments



For verifying the algorithm we proposed, we have done experiment of three simulations. These data were simulated with cortical surface constraints. Thus, in the first section, materials such as MR images, MEG instrument and cortical surface are described. The procedure of reconstructing cortical surface is consisted of three steps. It must be segmented by FreeSurfer, which is a set of software tools for study of cortical and subcortical anatomy, at first. Then, it is down sampled using VTK, which is a visualization toolkit and open source software for 3D computer graphics. Moreover, for easy observation of the cortical source distribution in sulcus, FreeSurfer is applied to inflate the down-sampled surface.

The first simulation is the simplest one that only one dipolar source was placed at a single position. Both the two approach using mixing and unmixing matrix were applied to the first simulation. Apparently, the unmixing matrix approach is much more accurate than mixing matrix approach. This is under our expectation. Thus, the imaging method must apply approach by unmixing matrix but the mixing matrix.

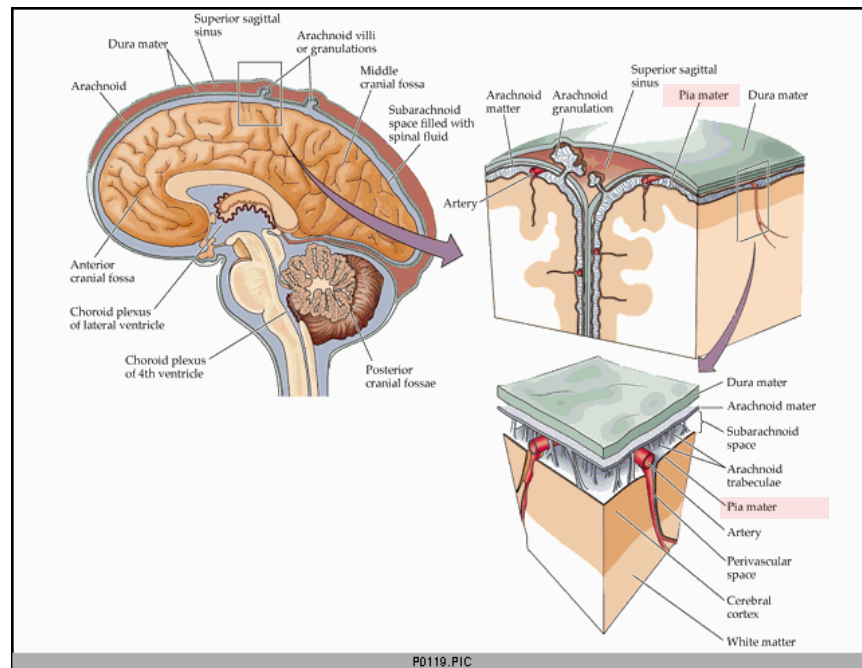
A tangent dipolar source is placed in simulation two for verify the accuracy of the imaging method since tangent should be separated better theoretically than sine when surrounding by lots of sine interferes. According to the experiment result, it is perfectly mapped to cortical surface because it is separated better than sines placed in the same place of the other simulations.

In the last simulation, it becomes much more complicated that four sources were placed at three location. It means there are two sources in one place. Moreover, one of these two sources was placed elsewhere. Even in the hard condition, the imaging method still works fine. The more detail are described in the following sections.

4.1 Materials

4.1.1 3D MR Images

T1-weighted MR head images were acquired on a 1.5 Tesla GE MR scanner, using 3D-FSPGR pulse sequence (TR = 8.67 ms, TE = 1.86 ms, TI = 400 ms, NEX = 1, flip angle = 15°, bandwidth = 15.63 kHz, matrix size = 256 × 256 × 124, voxel size = 1.02 × 1.02 × 1.5



(www.arts.uwaterloo.ca/~bfleming/psych261/)

Figure 4.1: **Surface of Brain.**

(This picture is excerpted from <http://www.arts.uwaterloo.ca/~bfleming/psych261/>)

The two kinds of surfaces reconstructed by FreeSurfer are pia mater and white matter. According to the physiological knowledge, pia mater closely envelopes the entire surface of the brain and is the closest one of these two reconstructed surface to the cortex. Thus, it is the picked physiological constraints of the proposed method for imaging of brain activities.

mm³).

4.1.2 Cortical Surface Reconstruction

Estimation of the proposed imaging method is based on physiological source constraints that brain activities locate on cortical surface with orientations, or said the surface normal, perpendicular to the surface. On the other hand, the informations of cortical surface are the prior knowledge.

The cortical surface is segmented using FreeSurfer [9] which is a set of software tools for study of cortical and subcortical anatomy. FreeSurfer segments the 3D volume data, MR image, into two kinds of surface that are pia mater and white matter representing by

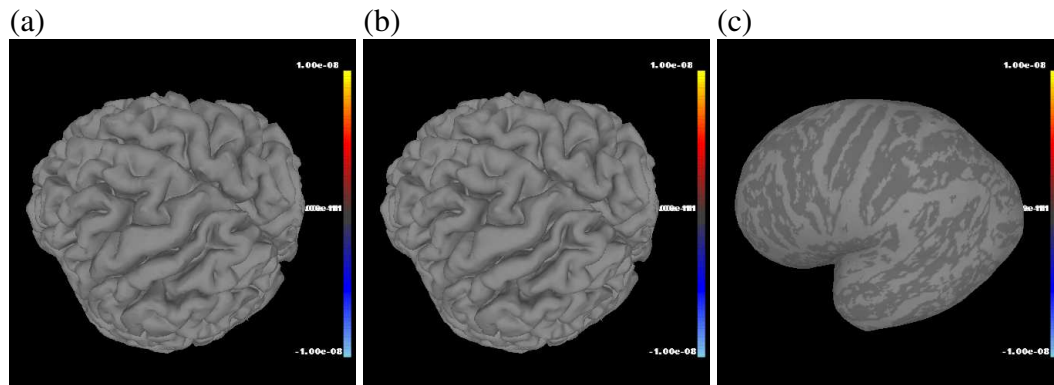


Figure 4.2: **Reconstructed Pia Mater** (a) Pia mater has been down sampled by 50% and 114,024 triangular points remain. (b) The original pia mater, composed of 228,044 triangular points, reconstructed by FreeSurfer. (c) The down sampled surface is inflated by FreeSurfer for clearly displaying the cortical source distribution. Gyrus is colored in gray and sulcus is colored in dark gray.

triangle meshes and each of them formed by a set of triangular points.

According to the physiological knowledge, electromagnetic fields are generated by a layer of pyramid cells in the cortex and pia mater is the closest one of the three kinds of brain surface outside the cortex, where the other ones are dura mater and arachnoid mater, to the cortex (Fig. 4.1). Hence, we pick the pia mater which closely envelopes the entire surface of the brain as the physiological constraint.

However, there are 228,044 points formed the triangle mesh of reconstructed pia mater (Fig. 4.2(b)). For easy calculation but with the tolerable distortion and non-smoothness, the pia mater surface is down sampled by 50% using VTK which is a visualization toolkit and open source software for 3D computer graphics. Thus, there are 114,024 points remained for our dipolar source imaging method (Fig. 4.2(a)). Moreover, the down sampled surface was inflated by FreeSurfer for displaying cortical surface clearly, especially for sulcus colored in dark gray (Fig. 4.2(c)).

4.1.3 MEG Device

The simulations were generated according to the device information from a real MEG measurement. The measurement was acquired by a whole head MEG system "Neuromag

Vectorview 306” which belongs to Taipei Veterans General Hospital. The MEG system is placed in a magnetically shielded room and has the capability of 306 channels simultaneously recording at 102 distinct sites, 24 bits analog to digital conversion, and up-to-8 kHz sampling rate which is sufficient to probe the fast dynamics inside human brain.

4.1.4 Data Preprocessing

For low SNR, it results from the much smaller scale of electrophysiological signal than of environmental noises. For instance, the magnitude of omnipresent static field of earth is around 10^{-1} Tesla and is much larger than of the induced magnetic field which is around 10^{-10} to 10^{-15} Tesla. In addition, MEG and EEG signals are often corrupted with the background brain activities and artifacts, such as the heartbeat, eye-blink, and environmental noises. Thus, data preprocessing is required for noise reducing.

Independent Component Analysis (ICA) are some commonly adopted techniques for increasing the SNR or rejecting artifacts. ICA was originally proposed for the purpose of blind source separation to find components that are mutually statistical independent [20]. It performs best when raw or unaveraged signals are applied as inputs. Recently, it has been proved a useful tool in neurological brain research and is widely-used for analyzing MEG/EEG signals [17, 18], especially for removing artifacts based on its independence assumption [3, 7, 16, 21]. In the following experiments, the first-stage ICA is applied for noises removal in both simulation and real data. Moreover, for selecting useful trials from real data, Signal-space-project (SSP) and EOG rejection is applied.

4.2 Experiments

As aforementioned in Section 2.2, simulation uses the forward solution with spherical head model. And according to the electrophysiological basis, the MEG/EEG sensors are most sensitive to the electromagnetic field with orientation that lying on the tangential plane of the spherical shell. Therefore, the dipolar sources in our simulations are placed at sulcus but not at gyrus and then the dipole orientations are almost tangential.

Three simulations were generated. Each of them was added 3000 random dipoles, or

said the background noises, with standard deviation 0.1 nAm within the sphere with radius of 7 cm and was simulated 10 trials in 1,001 sampling rate. Each trial was 1 second long. The analysis steps follow the work flow described in chapter 3 by Figure 3.1

The first simulation is the simplest case that a single sine dipolar source is placed. The second one places two dipolar sources, where one is a sine wave and the other is a tangent wave, at two distinct positions. ICA performs well in the first two simulations. The given dipolar sources are almost perfectly identified and the cortical distributions are agreeable to the ground truth.

In the last simulations, four dipolar sources are placed at three distinct positions where two of them are the same sine waves but differed in amplitudes and locations and the others are two sine waves with different frequencies located at two distinct places. ICA also performs well to identify three different time courses but one of them with additive leakage from another component. But even with the leakage, the proposed method still produces an agreeable imaging of cortical distributions.

The accuracy is examined by location error and similarity of temporal activities. Location error is represented by distance between location of the peak of cortical source distribution and of the ground truth. Similarity between the given sources and picked components is represented by correlation coefficient $corr(\mathbf{x}_i, \mathbf{x}_j) = (\mathbf{x}_i \cdot \mathbf{x}_j) / (\|\mathbf{x}_i\| \|\mathbf{x}_j\|)$. The smaller location error and the higher similarity it has, the more accurate it is.

4.2.1 Simulation 1 - A Single Sine Dipolar Source

Ground Truth

In the first simulation, Figure 4.4 shows the ground truth that a 15 Hz sine wave (4.4(c)) is placed at $\mathbf{r}_1 = (-29.47, 49.14, 94.75)$ mm and oriented to $\mathbf{q}_1 = (0.80, -0.10, 0.60)$ in MEG head coordinates (4.4(a)). Figure 4.4(b) displays the respective lead field vector with parameter $\theta_1 = \{\mathbf{r}_1, \mathbf{q}_1\}$. Figure 4.3 is the simulated measurement and the distribution to MEG sensors, so called a topography, at 250 ms which is the peak time. The distribution of measurements to sensors at peak time is similar to the given lead field and is agreeable to our expectation.

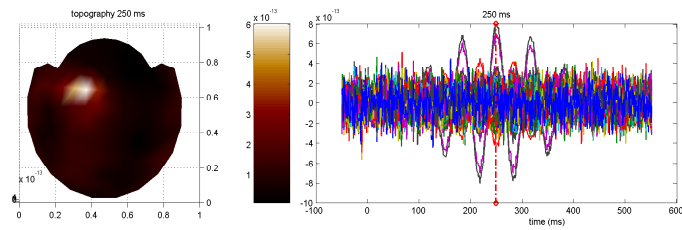


Figure 4.3: **Simulation 1 - The Output Measurement and Topography at 250 ms**

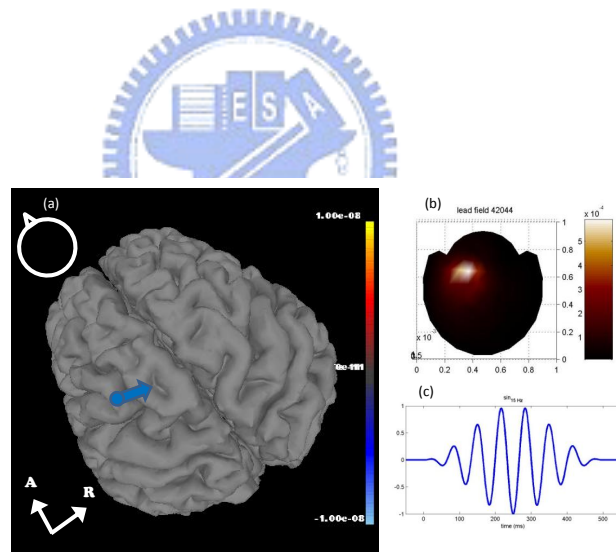


Figure 4.4: **Simulation 1 - Ground Truth.** (a) The location r and orientation q of the dipolar source are indicated by the blue arrow. In the right panel, (b) lead field vector of the source with parameter $\theta = \{r, q\}$ and (c) the 15 Hz sine wave are displayed.

No.	Method	Similarity of Temporal Activities	Location Error (mm)
1	$(\mathbf{B} = \mathbf{WL})^+$	0.9954	4.67
1'	$\mathbf{B} = \mathbf{L}^+ \mathbf{A}$	0.9954	127.73

Table 4.1: **Simulation 1 - Location Error and Similarity.** The spatiotemporal imaging of the two interested components are almost perfectly fit the ground truth.

ICA result

There are 105 independent components extracted from input measurement by the first-stage ICA (Fig. 4.5). And then reconstruct measurement by 1 interested component, which is closely correlated to the given source for simulation, and the respective mixing vector. Finally, the second-stage ICA outputs 1 interested component and it is picked to be mapped to cortical surface.



Cortical Source Distribution

There is 1 component regarded as the given source (Fig. 4.7(a)) and the respective cortical distribution (Figure 4.7(c)) displayed in both cortical surface and the inflated surface of the left hemisphere. The two figures in the bottom with green arrow and point that indicate the ground truth. Consequently, the cortical distribution demonstrates that the picked component was activated around the highlighted area and the location of peak of this distribution is close to the ground truth at distance of 4.67 mm.

Here we verify the two approach solving cortical source distribution of the same component by mixing and unmixing matrix according to Equation 3.1 and 3.3. The results are displayed in Figure 4.7 and 4.8 with respect to the unmixing matrix approach and mixing matrix approach. Apparently, the later performs awful even that the ground truth had been found but the most activated region was far way from the ground truth with 127.73 mm location error (Table. 4.1).

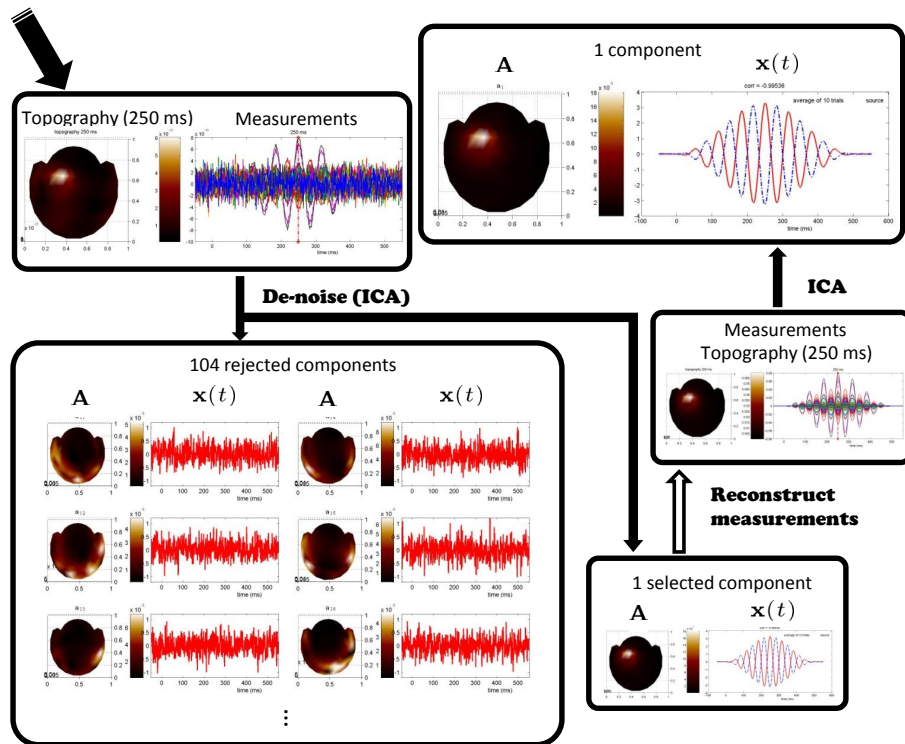


Figure 4.5: **Simulation 1 - ICA Decomposition.** There are 105 components output but only 1 interested component according to the first-stage ICA.

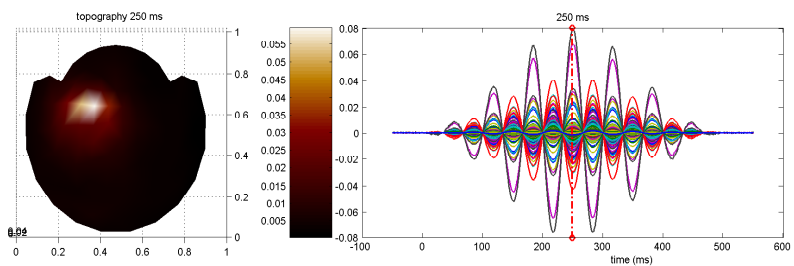


Figure 4.6: **Simulation 1 - the reconstructed measurement and topography by 1 selected ICA output components**

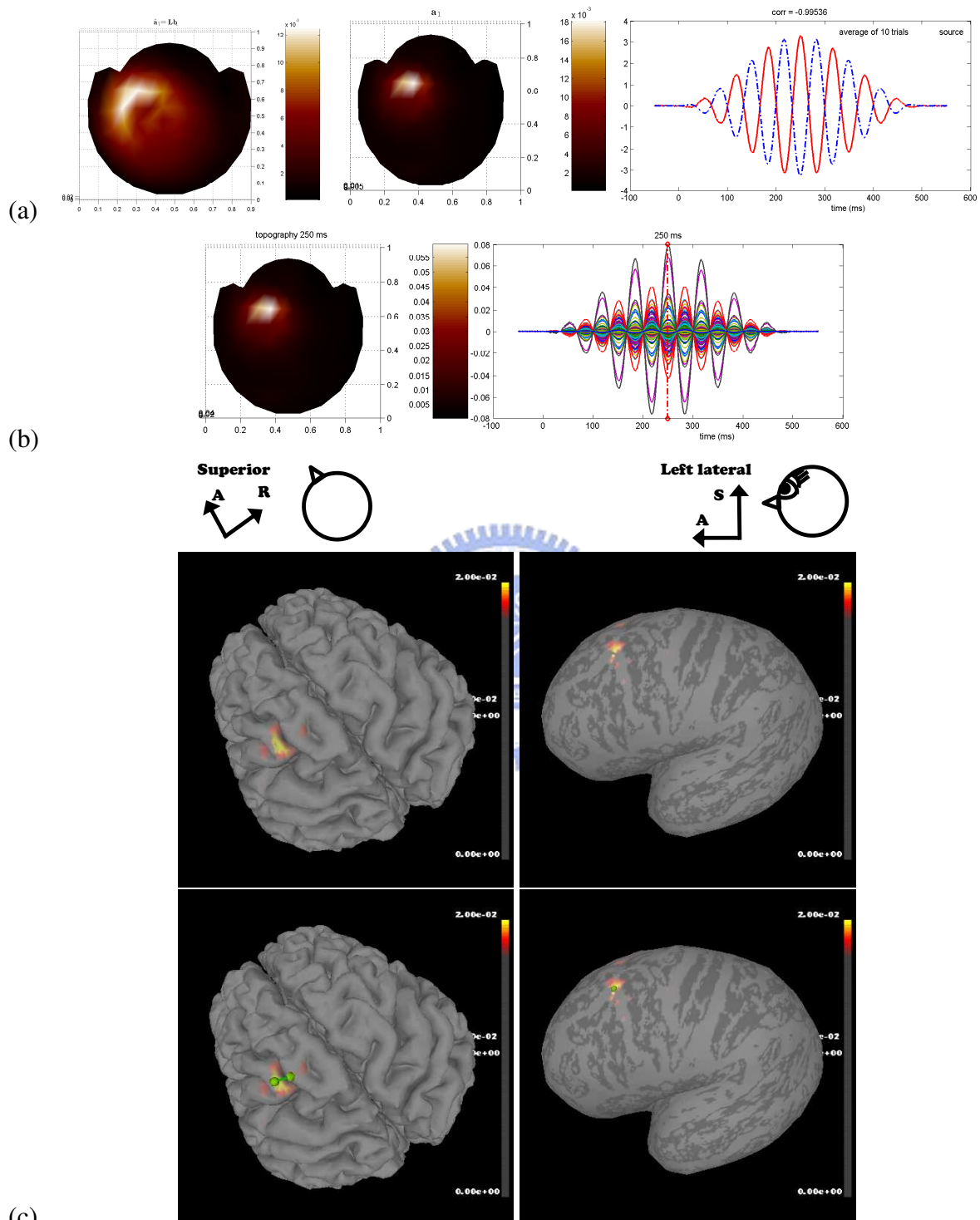


Figure 4.7: **Simulation 1 - Cortical Source Distribution Using Unmixing Matrix Approach.** (b) The interested component in red, closely correlated to the given source in blue, extracted by the 2nd-stage ICA and its topography. The left-most picture represents the reconstructed mixing vector $\hat{a}_1 = Lb_1$. (b) The measurement and topography at 250 ms which is reconstructed by 1 component, extracted by the 1st-stage ICA, and the respective mixing vector (c) Cortical source distribution b_1 . The green arrow and point indicate the ground truth. Location of the peak of b_1 and ground truth are at distance of 4.67 mm.

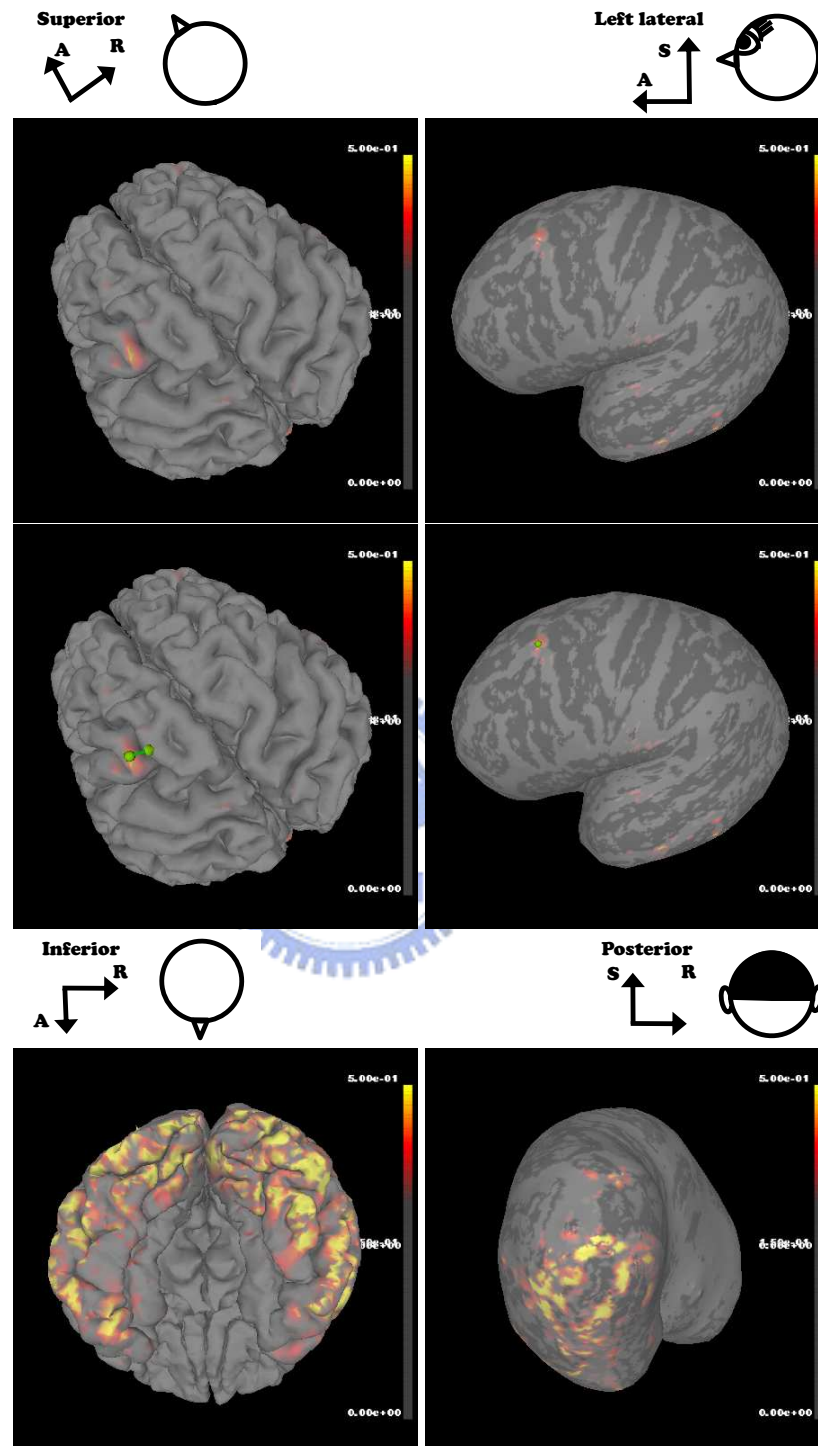


Figure 4.8: **Simulation 1 - Cortical Source Distribution Using Mixing Matrix Approach.** Cortical source distribution \mathbf{b}_1' . The green arrow and point indicate the ground truth. The region with strongest activation is located at inferior (the bottom two pictures) that is far away from the ground truth. Location of the peak of \mathbf{b}_1' and ground truth are at distance of 127.73 mm.

		Location r_i (mm)			Orientation q_i		
		x	y	z	x	y	z
(a)	i						
	1	-29.47	49.14	94.75	0.80	-0.10	0.60
	2	-34.90	-18.64	89.52	0.80	0.12	0.59

Sources

(c)	No.	Fig. 4.10	waveform	location	freq. (Hz)	duration (ms)	strength (nAm)
	1	(b)	tangent	r_1	11	0–500	1.0
	2	(c)	sine	r_2	15	0–500	1.0

Table 4.2: **Simulation 2 - Ground Truth** Two dipolar sources were placed at (a) two distinct locations and the distances between the two locations are listed in the right panel. (b) Table on the bottom lists information of dipolar sources including location, frequency, and duration. (See Fig. 4.10)

4.2.2 Simulation 2 - Two Uncorrelated Dipolar Sources

Ground Truth

Two uncorrelated dipolar sources, 11 Hz tangent and 15 Hz sine wave, were placed in the second simulation. The ground truth is listed in table 4.2 and displayed in Figure 4.10. The simulated measurement and topography for 250 ms is shown in Figure 4.9 which is similar the to the given lead field vector l_{θ_2} (Figure 4.10(c)).

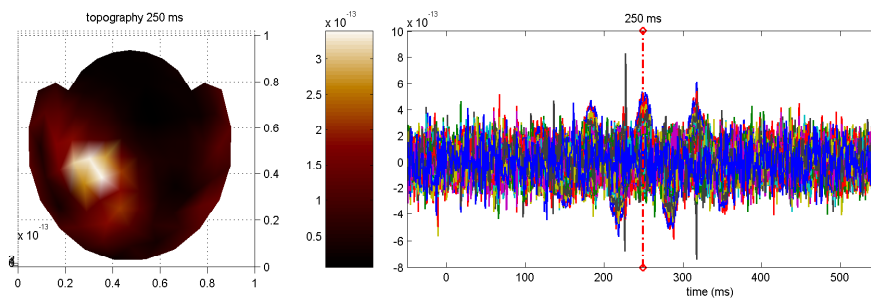


Figure 4.9: **Simulation 2 - The Output Measurement and Topography**

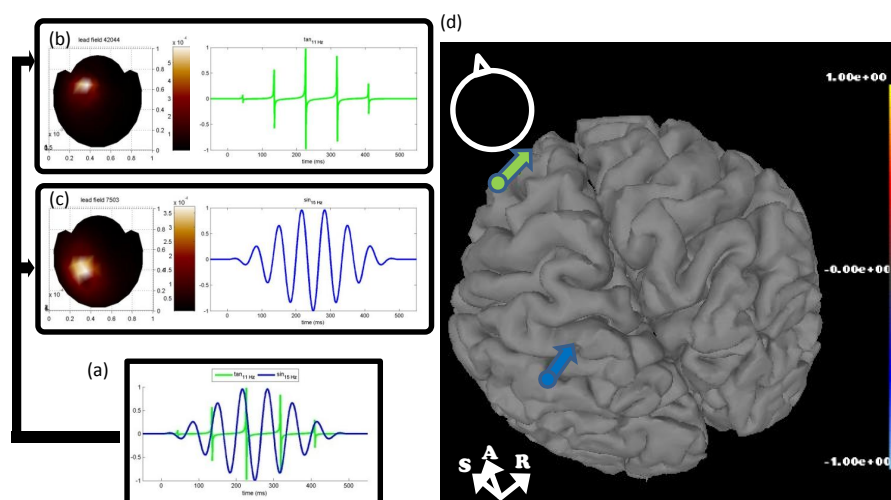


Figure 4.10: **Simulation 2 - Ground Truth.** (a) Two kinds of sources. (b) 11 Hz tangent dipolar source and the respective lead field with parameter $\theta_1 = \{\mathbf{r}_1, \mathbf{q}_1\}$ indicated by the green arrow. (c) 15 Hz sine dipolar source and the respective lead fields with parameter $\theta_2 = \{\mathbf{r}_2, \mathbf{q}_2\}$ indicated by the blue arrows. (d) Ground truth on cortical surface.



ICA result

There are 93 independent components extracted from input measurement by the first-stage ICA (Fig. 4.11). And then reconstruct measurement by 2 interested component, which are closely correlated to the given sources, and the respective mixing vector. Finally, the second-stage ICA outputs 2 component and they are picked to be mapped to cortical surface.

Cortical Source Distribution

There are 2 components regarded as the given sources (Figure 4.12(a) and Figure 4.13(a)) and the respective cortical distribution (Figure 4.12(c) and Figure 4.13(c)) displayed in both cortical surface and the inflated surface of the left hemisphere. The two figures in the bottom with green arrow and point that indicate the ground truth. In this simulation, the spatiotemporal imaging of the two components are almost perfectly fit the ground truth with small location errors with location error less than 1 mm (Table 4.3).

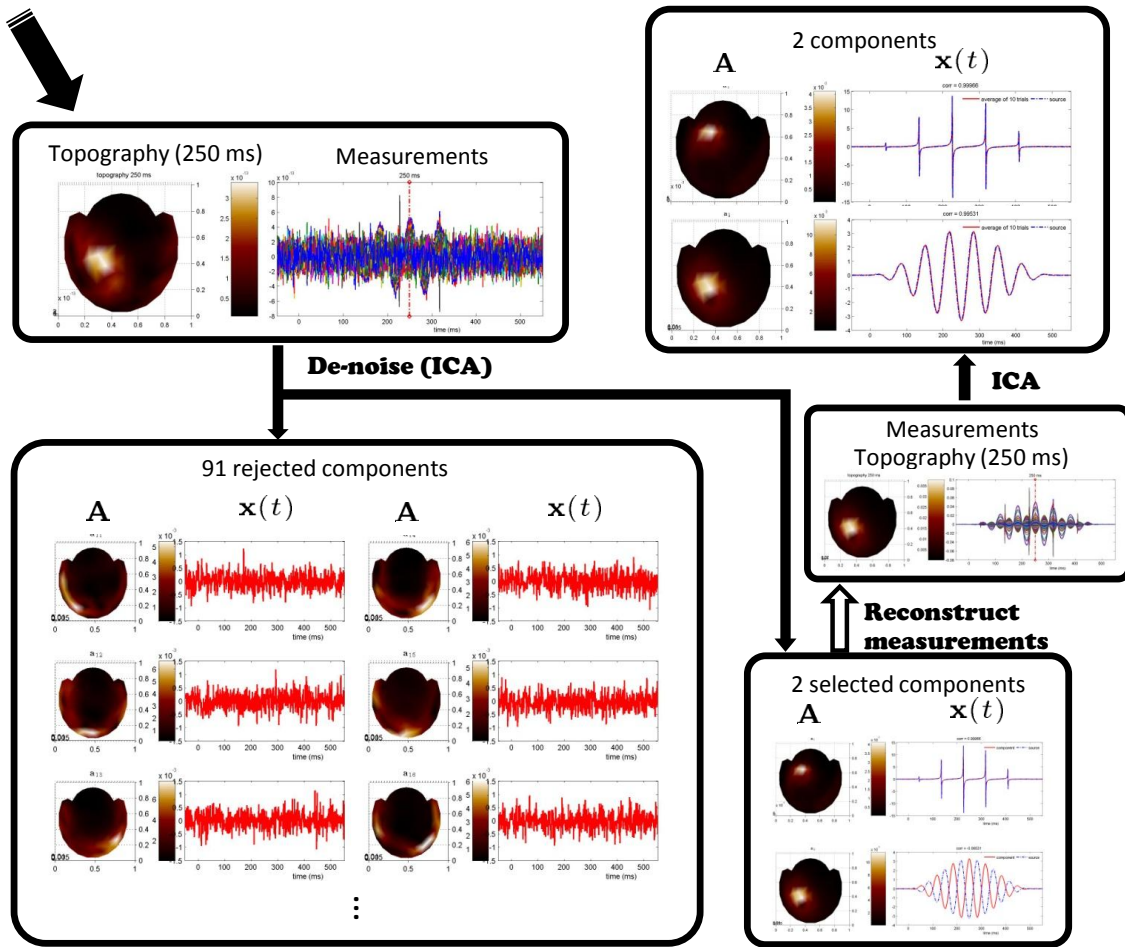


Figure 4.11: **Simulation 2 - ICA Decomposition.** There are 93 components output but only 2 interested component according to the first-stage ICA.

No.	Wave	Freq. (Hz)	Similarity of Temporal Activities	Location Error (mm)
1	tangent	11	0.9997	0.00
2	sine	15	0.9953	0.91

Table 4.3: **Simulation 2 - Location Error and Similarity.** The spatiotemporal imaging of the two interested components are almost perfectly fit the ground truth.

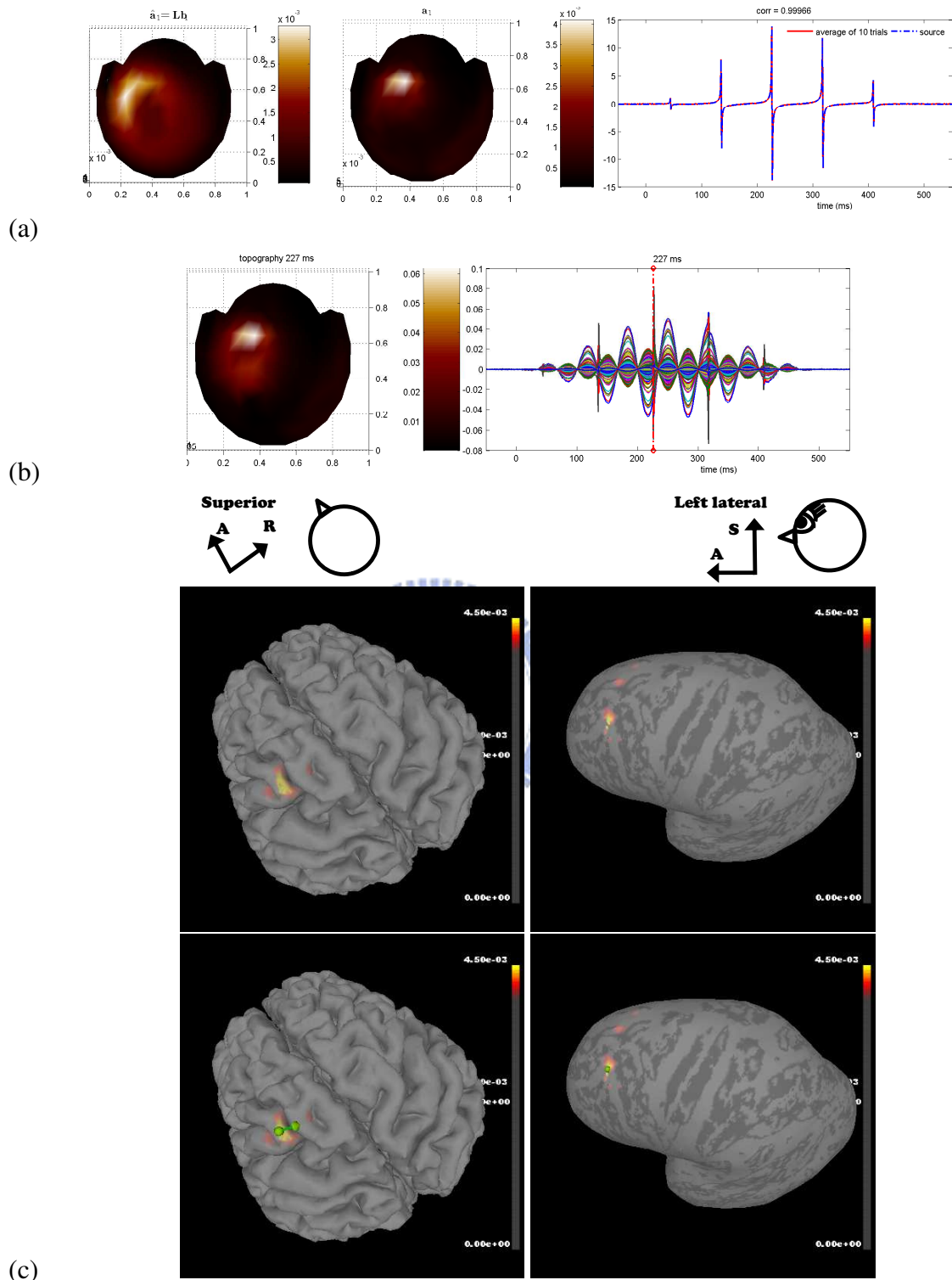


Figure 4.12: **Simulation 2 - Cortical Distribution of the 1st component.** (a) The output component and its topography is compared to the given tangent source. The left-most picture represents the reconstructed mixing vector $\tilde{a}_1 = \mathbf{Lb}_1$. (b) According to the reconstructed measurement, topography for 227 ms which is the peak time the tangent source but with weaker activation of the other source. (c) According to the cortical distribution, the strongest activation of the tangent component is exactly located at the ground truth position.

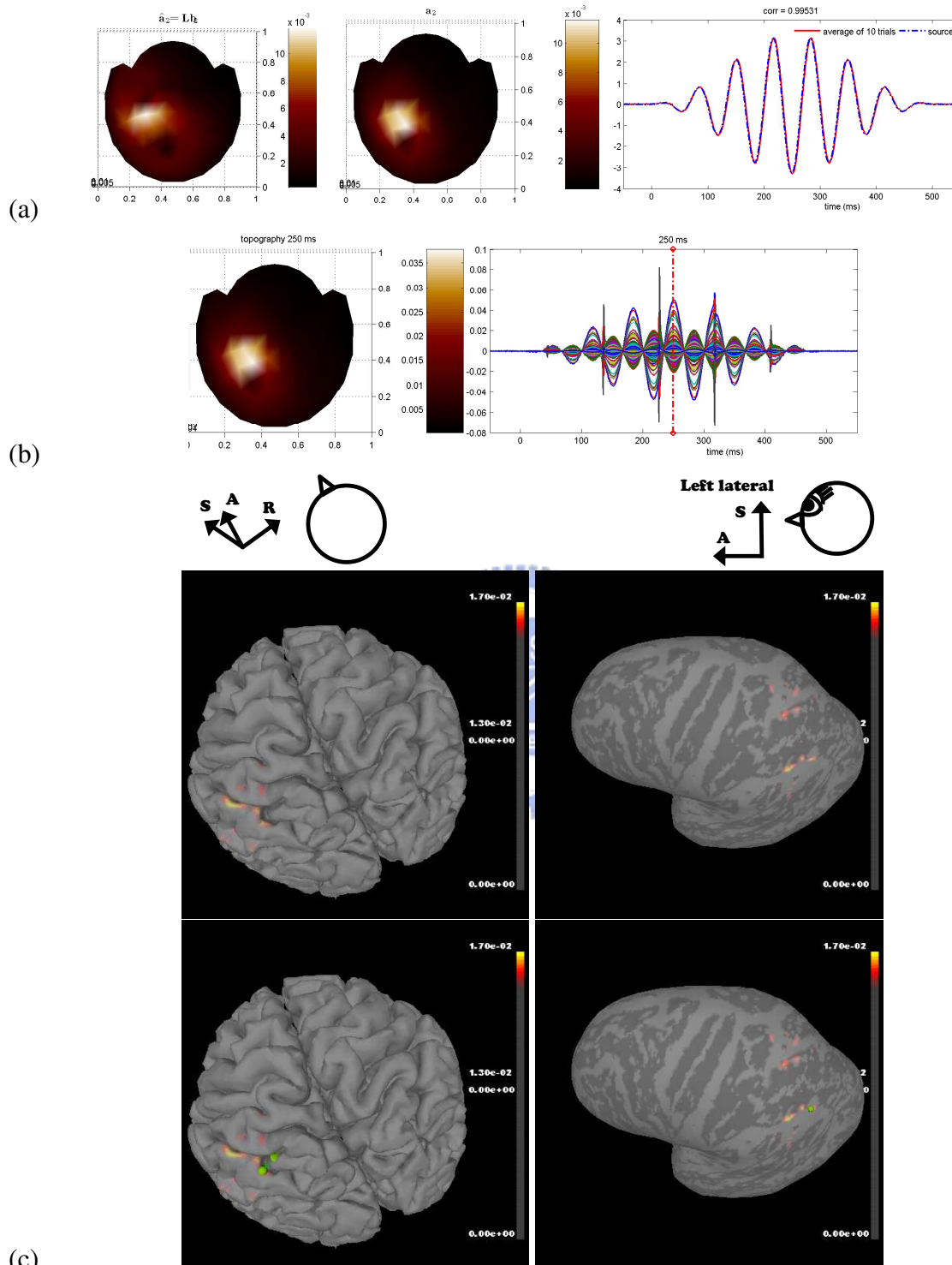


Figure 4.13: **Simulation 2 - Cortical Distribution of the 2nd component.** (a) The output component and its topography is compared to the given sine source. The left-most picture represents the reconstructed mixing vector $\hat{a}_2 = Lb_2$. (b) According to the reconstructed measurement, topography for 250 ms which is the peak time the sine source but with weaker activation of the other source. (c) According to the cortical distribution, the strongest activation of the sine component is located around the ground truth position in distance of 0.91 mm.

	Location \mathbf{r}_i (mm)			Orientation \mathbf{q}_i			Distance $\ \mathbf{r}_i - \mathbf{r}_j\ $			
	i	x	y	z	x	y	z	$i \setminus j$		
(a)	1,3	-29.47	49.14	94.75	0.80	-0.10	0.60	2	4	
	2	-26.82	-0.36	105.64	0.83	0.45	0.34	1,3	50.75 50.90	
	4	23.63	35.00	98.09	0.94	0.08	-0.34	2	63.32	
Sources (sine)										
No.	Figure 4.15	wave color	location	freq. (Hz)	duration (ms)	strength (nAm)				
(c)	1	(b)	green	\mathbf{r}_1	7	0–500	0.3			
	2	(c)	blue	\mathbf{r}_2	17	50–350	0.5			
	3	(b)	red	$\mathbf{r}_3 = \mathbf{r}_1$	31	0–200	0.7			
	4	(d)	red	\mathbf{r}_4	31	0–200	1.0			

Table 4.4: **Simulation 3 - Ground Truth** Four dipolar sources were placed at (a) three distinct locations and the distances between the three locations are listed in the right panel. (b) Table on the bottom lists information of dipolar sources including location, frequency, and duration. (See Figure 4.15)

4.2.3 Simulation 3 - Four Sine Dipolar Sources

Ground Truth

In the third simulation, Figure 4.15 and Table 4.4 shows the ground truth that four dipolar sources are placed at three distinct positions which means two of the sources, the first and the third one, are at the same location.

In Figure 4.15, temporal activities and locations of the four dipolar sources are distinguished by colors and locations are numbered. temporal activity of the first source, a 7 Hz sine wave with duration 0-200 ms, in green (Figure 4.15(b)) is located where the green arrow numbered in 1 indicates (e). Temporal activity of the second source, a 17 Hz sine wave with duration 50-350 ms, in blue (Figure 4.15(c)) is located where the blue arrow numbered in 2 indicates (Figure 4.15(e)).

Temporal activities of the third and the fourth source, 31 Hz sine waves with duration 0-200 ms but with different strength 0.7 and 1 nAm, in red numbered in 3 and 4 (Fig-

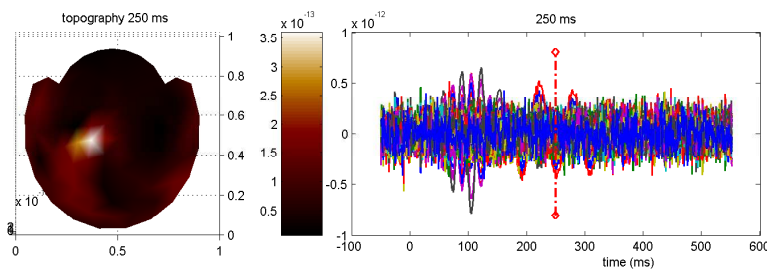


Figure 4.14: **Simulation 3 - The Output Measurements and Topography.** The simulated measurements contain 4 dipolar sources and 3000 random dipoles. The topography in 250 ms is displayed in the left panel and the peak is around the location of the given 17 Hz sine.

ure 4.15(c)) are located at two distinct positions. The weaker one is located at the same place as the 7 Hz sine in green and the stronger one is individually placed at location No. 3. The output measurements and topography in 250 ms are displayed in Figure 4.14.

ICA result

There are 105 independent components extracted from input measurement by the first-stage ICA (Figure 4.17). And then reconstruct measurement by 3 interested components (Figure 4.16), which is closely correlated to the given sources for simulation, and the respective mixing vectors. Finally, the second-stage ICA outputs 3 interested component and they are picked to be mapped to cortical surface.

See Figure 4.18 for more detail about the first component. There are three temporal activities plotted in the figure on top. The 1st output component is plotted with red solid line. The given 7 Hz sine is plotted with green dashed line. The similarity between temporal activities of the output component and the given 7 Hz sine is 0.9886. Look at the blue dashed line in figure on top, it represents the combination of 7 and 17 Hz sines, by 98.86% 7 Hz sine minus 10% 17 Hz sine, and its similarity between the component becomes higher to 0.9985. Apparently, this component is strongly correlated to 7 Hz sine but also receives a little leakage from 17 Hz sine at the later segment of temporal activity. In addition, the leakage effect can be observed from the mixing vector and lead field vector of the given 17 Hz sine, plotted in blue.

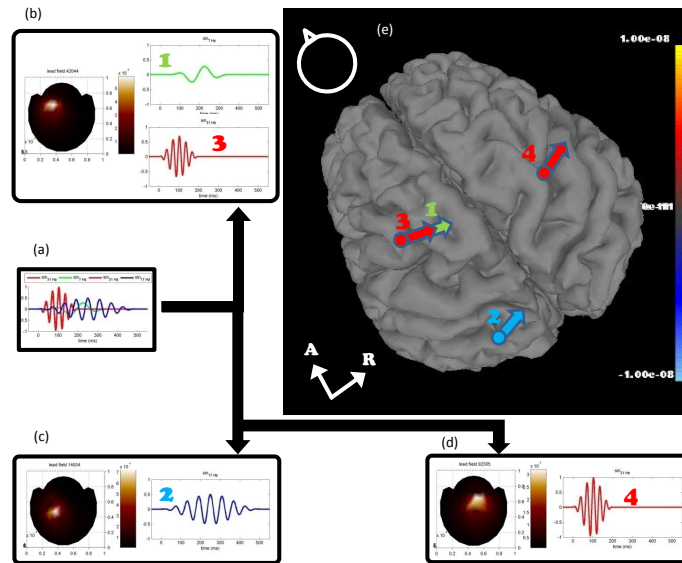


Figure 4.15: **Simulation 3 - Ground Truth.** (a) Three kinds of dipolar sources. (b) 7 Hz and 31 Hz dipolar sources with duration 50-350 ms and 0-200 ms. Topography is the respective lead field. Location and orientation of the two sources are indicated by the arrow both in red and green numbered in 1 and 3. (c) A 17 Hz sine dipolar sources with duration 0-500 ms and the respective lead field where location and orientation are indicated by the blue arrow numbered in 2. (d) A 31 Hz sine dipolar source with duration 0-200 ms and the respective lead fields where location and orientation are indicated by the red arrow numbered in 4. Attention that this 31 Hz sine is almost the same as the red one in (a) except that 31 Hz sine has stronger activation on this position than on the first position. (e) Ground truth on cortical surface.

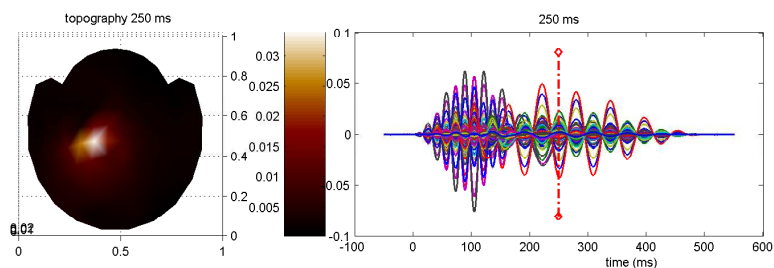


Figure 4.16: **Simulation 3 - the reconstructed measurement and topography** The measurements $m(t)$ were reconstructed by 3 selected components $x(t)$ the the respective mixing vectors A where $m(t) = Ax(t)$. (See Figure 4.17)

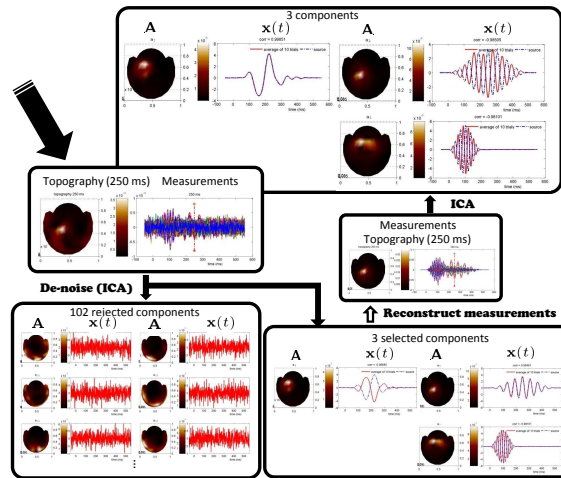


Figure 4.17: **Simulation 3 - ICA Decomposition.** After the first-stage ICA, there are 105 components output but only 3 interested components that closely correlated to the given sources. The similarity of temporal activities of given sources and components are listed in Table 4.5

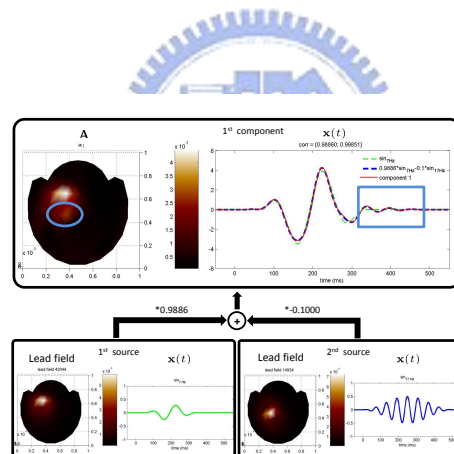


Figure 4.18: **Simulation 3 - Leakage of the 2nd Component.** There are three temporal activities plotted in the figure on top. The 1st output component is plotted with red solid line. The given 7 Hz sine is plotted with green dashed line. The similarity between temporal activities of the output component and the given 7 Hz sine is 0.9886. Look at the blue dashed line in figure on top, it represents the combination of 7 and 17 Hz sine sources, by 98.86% 7 Hz sine minus 10% 17 Hz sine, and its similarity between the component becomes higher to 0.9985. Apparently, this component is strongly correlated to 7 Hz sine but also receives a little leakage from 17 Hz sine at the later segment of temporal activity. In addition, the leakage effect can be observed from the mixing vector and lead field vector of the given 17 Hz sine, plotted in blue.

No.	Sine (Hz)	Similarity of Temporal Activities	Location Error (mm)
1	7 and 17	0.9985	3.64 and 2.18
2	17	-0.9851	3.62
3	31	-0.9810	3.38 and 0.00

Table 4.5: **Simulation 3 - Location Error of Cortical Source Distribution**

Cortical Source Distribution

There are 3 components (Figure 4.17) regarded as the given sources (Figure 4.15) and the respective cortical distribution (Figure 4.19–4.21) displayed in both cortical surface and the inflated surface of the left hemisphere.

It differs from the first two simulations that the first component shown in Figure 4.18 is not perfectly fit the given 7 Hz sine but also receives a little leakage from the 17 Hz sine. In addition, the leakage effect can also be observed from the corresponding mixing vector and the cortical distribution. In Figure 4.19, Cortical distribution of the 7 Hz sine, the main element of the first component, shows that it is activated around the left frontal, the ground truth. And 17 Hz, the other element, is activated around the left posterior met the ground truth in the distance of 4.67 mm.

Cortical source distribution of the second component, meets the given 17 Hz sine, is displayed in Figure 4.20. The 17 Hz sine was placed at a single position and the strongest activation of cortical distribution is around the location of the ground truth in the distance of 2.17 mm.

Unfortunately, the location error of the peak of cortical source distribution of the third component, meets the given 31 Hz sine, is 16.33 mm that much larger than the other components and the peak is located across the gyrus from the ground truth (Figure ??). This phenomenon is going to be discussed in the next chapter.

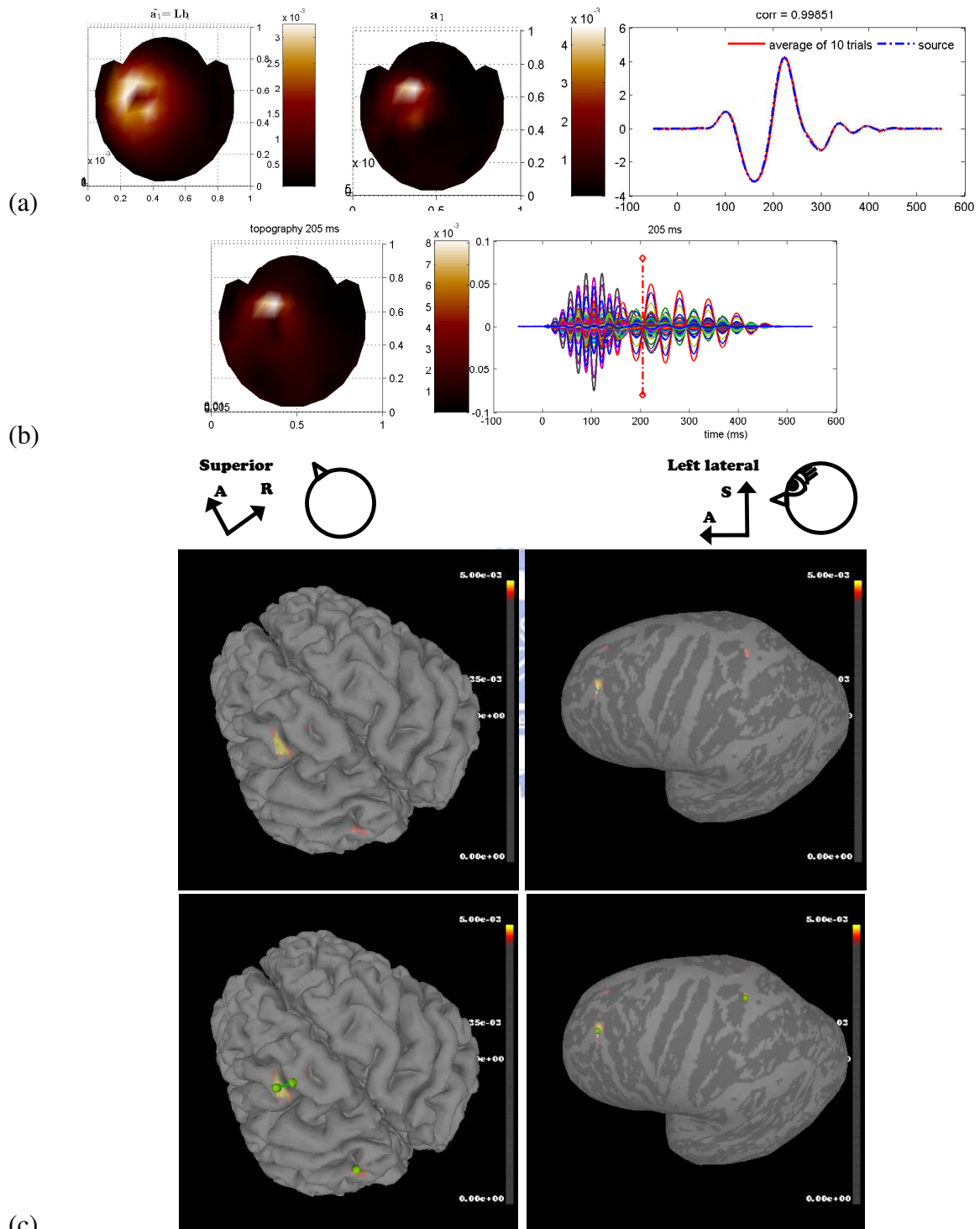


Figure 4.19: **Simulation 3 - Cortical Distribution of the 1st component.** (a) The output component and its topography is compared to the given sources. The left-most picture represents the reconstructed mixing vector $\tilde{a}_1 = \mathbf{L}b_1$. (b) Cortical distribution with strong activation at both ground truth location of 7 Hz near left frontal and 17 Hz sines in left posterior. Location of cortical distribution peak and the given 7 Hz sine is at distance of 3.64. Location of cortical distribution peak and the given 17 Hz sine is at distance of 2.18 mm.

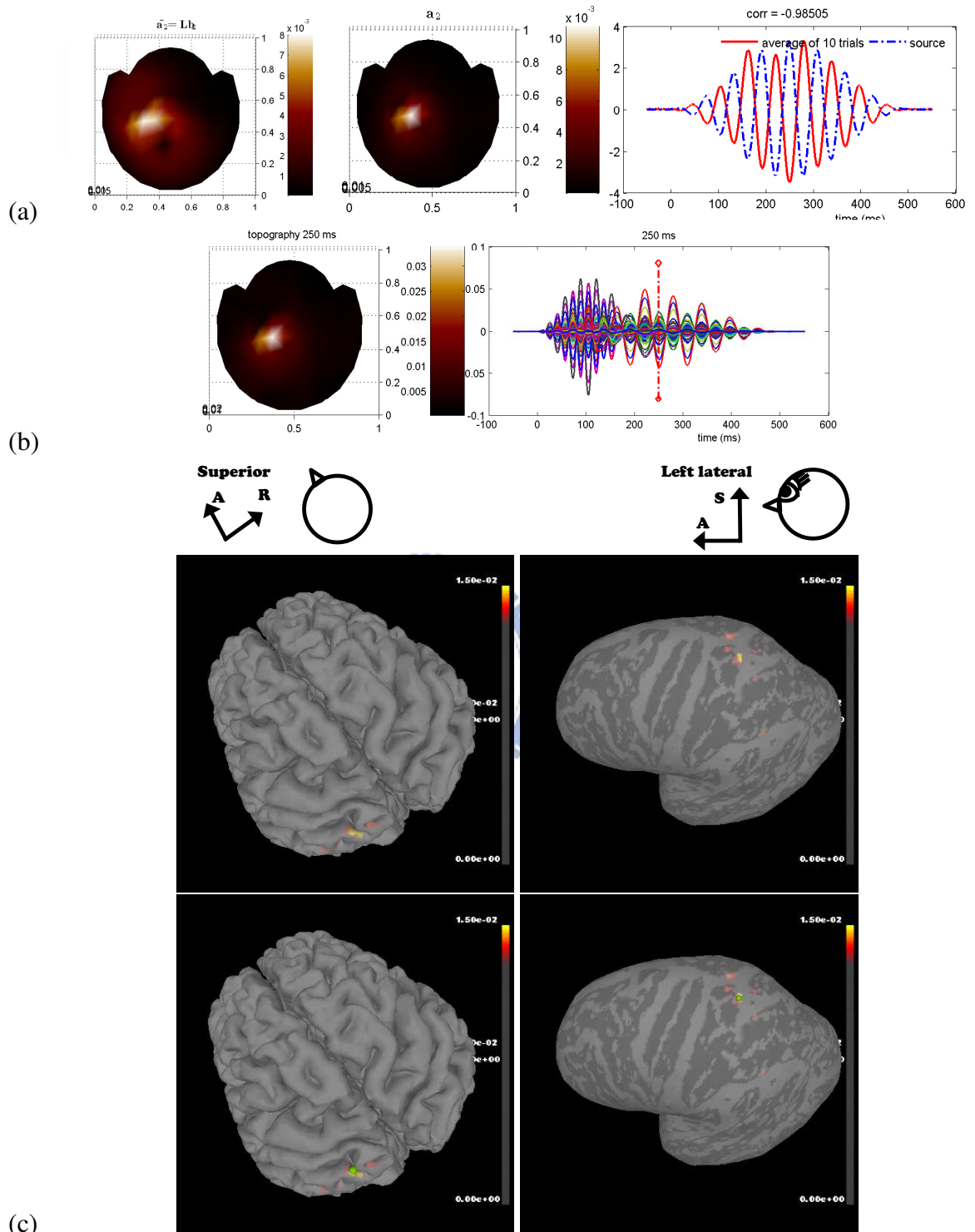


Figure 4.20: **Simulation 3 - Cortical Distribution of the 3rd component.** (a) The output component and its topography is compared to the given sources. The left-most picture represents the reconstructed mixing vector $\tilde{a}_2 = \mathbf{Lb}_2$. (b) Cortical distribution with strong activation around the ground truth location of 17 Hz sine in left posterior. Location of cortical distribution peak and the ground truth are at distance of 3.62 mm.

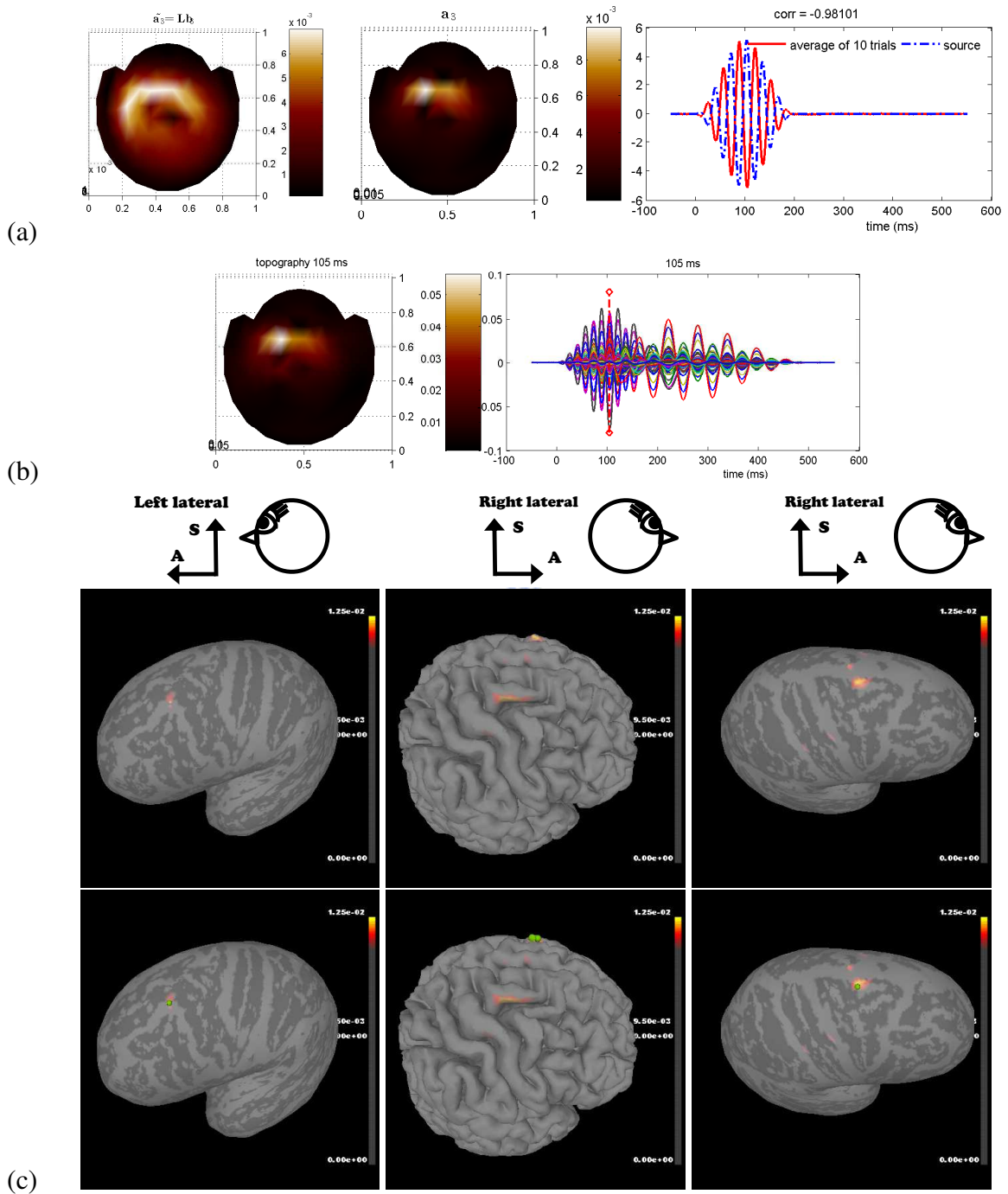


Figure 4.21: **Simulation 3 - Cortical Distribution of the 2nd component.** (a) The output component and its topography is compared to the given sources. The left-most picture represents the reconstructed mixing vector $\tilde{a}_3 = Lb_3$. (b) Cortical distribution with strong activation around the ground truth location of 31 Hz sine in right hemisphere. Location of cortical distribution peak and the ground truth are at distance of 3.38 and 0.00 mm.

4.2.4 Experiments of Gender Discrimination

We propose the method for imaging of independent components extracted using the standard ICA algorithms. Even though this method is neither for solving the inverse problem nor for more precisely decomposing independent component, but it has proved to be helpful and provides a both intuitive and efficient solution for mapping the discovered features or interested components of MEG/EEG signals to cortical surface. Consequently, the discovered features can be directly mapped to cortical surface without redo the experiments.

In this section, the experiment result and cortical source distributions are calculated from the real recordings. Bipolar Disorder (BD) patients and normal subjects were asked to specify the genders of presented faces that prevents the subject's explicit recognition or categorization of the emotion expressed. In the following subsections, the more detail of experiment paradigm will be described and we demonstrated the experiment result that calculated from the recording of angry condition of one normal subject.

Experiment Paradigm of Gender Discrimination

Twenty normal subjects and twelve bipolar disorder patients participate this experiment. Face images are gray-scaled photographs of faces, depicting neutral, angry, happy and sad. The task is to specify the gender of the presented faces that prevents the subject's explicit recognition or categorization of the emotion expressed. Subjects are instructed to lift the right or left index finger while recognizing the presented face image as female or male. For each condition, about 288 trials, 20 minutes are retrieved. The experiment paradigm is shown in Figure 4.22. Each stimulus is separated in 3000 ms by the sign of plus. First, one image of emotional face is displayed for 1500 ms. The following is 1000 ms blank. Then, a cue to ask subjects to response for male or female by image of the question mark for 500 ms.

ICA Result and Preprocessing

We analyze the recordings of angry condition of one normal subject that there are 60 trials and the duration of each trial is from 0 to 500 ms. The sampling rate is 1001 Hz

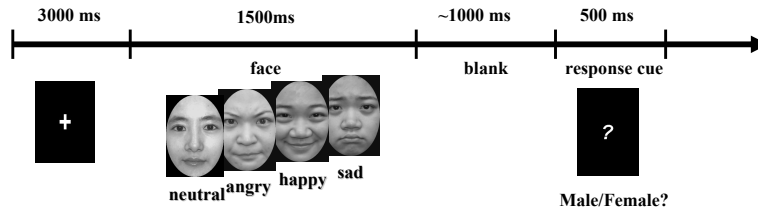


Figure 4.22: **Experiment Paradigm of Gender Discrimination.** The task is to specify the gender of the presented faces that prevents the subject's explicit recognition or categorization of the emotion expressed. Subjects are instructed to lift the right or left index finger while recognizing the presented face image as female or male. For each condition, neutral, happy, angry and sad, 20 minutes about 288 trials are retrieved. Each stimulus is separated in 3000 ms by the sign of plus. First, one image of emotional face is displayed for 1500 ms. The following is 1000 ms blank. Then, a cue to ask subjects to response for male or female by image of the question mark for 500 ms.



and thus there are 500 sample points of each trial. The flow-chart and result of ICA and preprocessing are shown in Figure 4.23 that all temporal activities are averaged out for 60 trials and plotted with duration of 0 to 200 ms except the top two pictures are plotted with duration of 0 to 500 ms. By the first-stage ICA as a de-noise step, there are 193 independent components extracted from input measurement. Then, reject 154 components by kurtosis value $\mathbf{v} \in \mathbb{R}^{193}$ of each component [3] and thus 39 components remain. Components are rejected if $\|v_i - v_{mean}\| \geq 1.7 \times v_{std}$ where v_i is the kurtosis value of the i^{th} component, v_{mean} is mean of \mathbf{v} and v_{std} is the standard deviation of \mathbf{v} . The number of output components in second-stage ICA is also 39. Moreover, preprocessing steps, like band-pass filter and baseline correction, are applied to temporal activities of all 39 components. The pass band is from 2 to 50 Hz. Mean values of temporal activities during 350 to 450 ms, indicated by with red frame of the image on left-top side (Figure 4.23), are used for baseline correction. Then, these preprocessed components are all mapped to cortical surface.

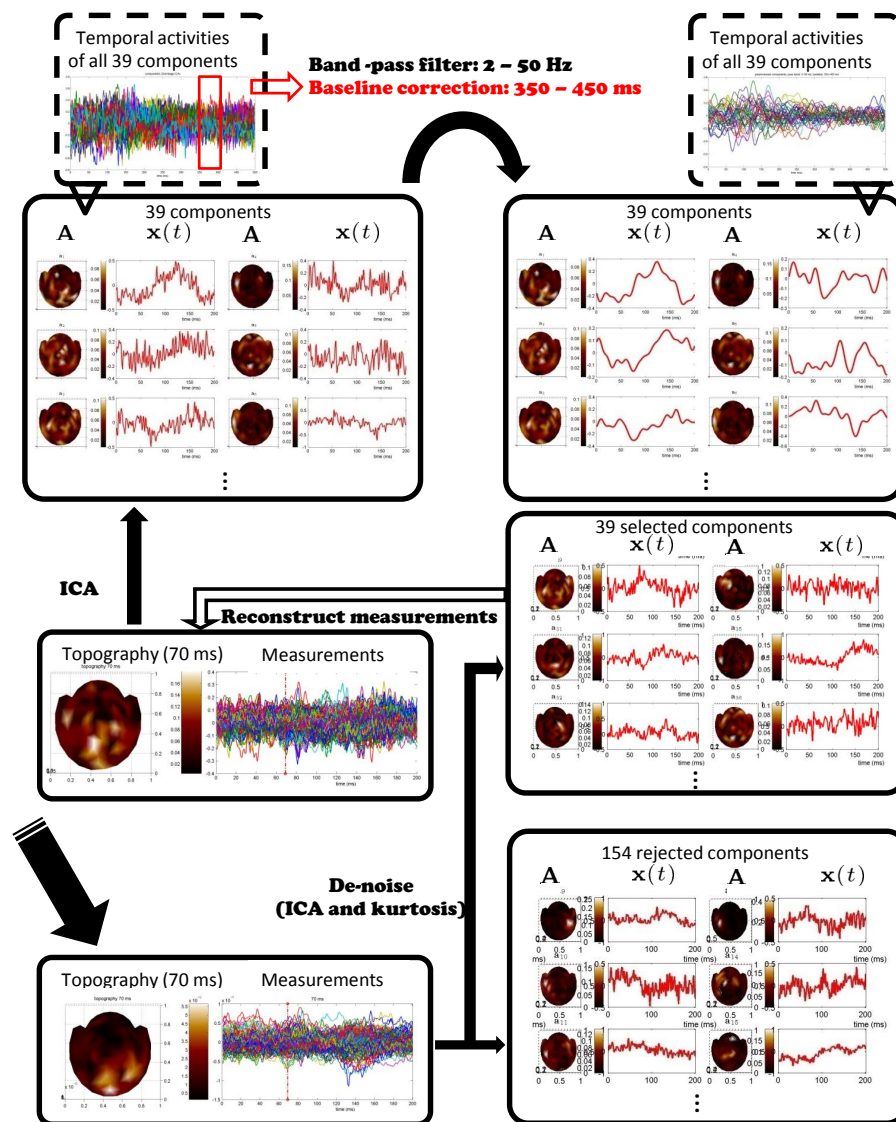


Figure 4.23: **ICA Result of Real Data.** We analyze the recordings of angry condition of one normal subject that there are 60 trials and the duration of each trial is from 0 to 500 ms. The sampling rate is 1001 Hz and thus there are 500 sample points of each trial. This figure shows the flow-chart and result of ICA and preprocessing that all temporal activities are averaged out for 60 trials and plotted with duration of 0 to 200 ms except the top two pictures are plotted with duration of 0 to 500 ms. There are 193 independent components extracted from input measurement by the first-stage ICA. Then, 154 components are rejected using kurtosis and 39 components remain. Moreover, preprocessing steps, like band-pass filter and baseline correction, are applied to temporal activities of all 39 components. The pass band is from 2 to 50 Hz. Mean values of temporal activities during 350 to 450 ms, indicated by with red frame of the image on left-top side, are used for baseline correction.

Lead Field

It has been revealed that cortical constraint is help for improving imaging method, such as beamformer, if the co-registration and segmentation errors are smaller than 2 mm and 10° [14]. Otherwise, even small errors in anatomical constraints can give rise to large errors in source reconstructions. Moreover, the higher spatial resolution it is, the worse effects it has.

Thus, to avoiding the effects resulted from errors in anatomical constraints, dipole orientations used in the forward model must be determined on the other way. In this experiment, dipole orientations are estimated using the maximum contrast beamformer (MCB) [5]. Before apply MCB to measurements, a few steps of data preprocessing are performed. First, 70 trials remain after EOG rejection and filtered by SSP matrix. Then, baseline correction is performed using mean of signals during -300 to -100 ms and the pass band are 2 to 50 Hz. The spatial filter is calculated using control state from -300 to -100 ms and active state from 35 to 235 ms. The trade-off value α is 0.02. The active state of f-statistic map is from 85 to 185 ms.

Cortical Source Distribution

According to the cortical source distributions (Figure 4.25–4.34), the 39 components are separated in to eight groups that strongly activated in auditory area, frontal cortex, V3, supplementary (SMA) and motor area, motor area, somatosensory area, SMA and Wernicke's area. In each figure, temporal activities averaged out for 60 trials with duration 0 to 200 ms, topographies or said mixing matrix \mathbf{A} , reconstructed topographies $\tilde{\mathbf{A}} = \mathbf{L}\mathbf{B}$ by lead field matrix \mathbf{L} , tomographies \mathbf{B} or said the cortical source distribution shown in left-lateral, superior and right-lateral view are displayed in the order from left to right for a single group.

There are two components, numbered in 6 and 32, in the first group with strong activations in the left and right auditory area (Figure 4.25). There is only one component, numbered in 5, in the second group that is strongly activated in the right frontal cortex (Figure 4.26). There are three components, numbered in 4 and 13, in the third group with strong activations in V3 area which is part of the occipital lobe cortex (Figure 4.27). There

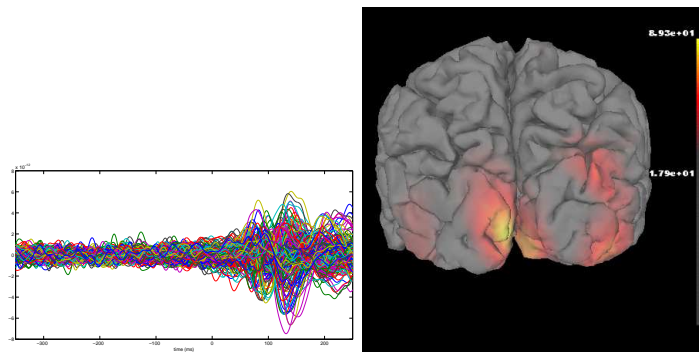


Figure 4.24: **Preprocessed Measurements and Cortical Source Distribution Calculated by MCB of Real Data.** Before apply MCB to measurements, a few steps of data preprocessing are performed. First, 70 trials remain after EOG rejection and filtered by SSP matrix. Picture in the left panel is the preprocessed measurements, plotted during -350 to 250 ms, that the pass band are 2 to 50 Hz and the duration of baseline correction is from -300 to -100 ms. Then, the dipole orientations for calculating lead field matrix are estimated using MCB. The spatial filter is calculated using control state from -300 to -100 ms and active state from 35 to 235 ms. The trade-off value α is 0.02. The active state of f-statistic map is from 85 to 185 ms. The f-statistic map in posterior view is shown in the right panel with strong activation in left occipital cortex.

are two components, numbered in 20 and 27, in the fourth group with strong activations in both the supplementary (SMA) and primary motor cortex that played a role in planning of complex and movement coordination (Figure 4.28). There are five components, numbered in 3, 15, 21, 28 and 39, in the fifth group with strong activations in the primary motor cortex around the central sulcus (Figure 4.29). There are six components, numbered in 9, 11, 12, 23, 24 and 38, strongly activated in the somatosensory cortex that believed in visuomotor coordination (Figure 4.30). There are six, numbered in 2, 7, 17, 18, 25 and 35, components in the seventh group strongly activated in the somatosensory cortex that believed in visuomotor coordination (Figure 4.31). In the last group, the eighth one and the biggest one, shown in Figure 4.32, 4.33 and 4.34, there are fifteen components, numbered in 1, 8, 10, 14, 16, 19, 22, 26, 29, 30, 31, 33, 34, 36 and 37, strongly activated in Wernicke's area involved in the understanding and comprehension of spoken language.

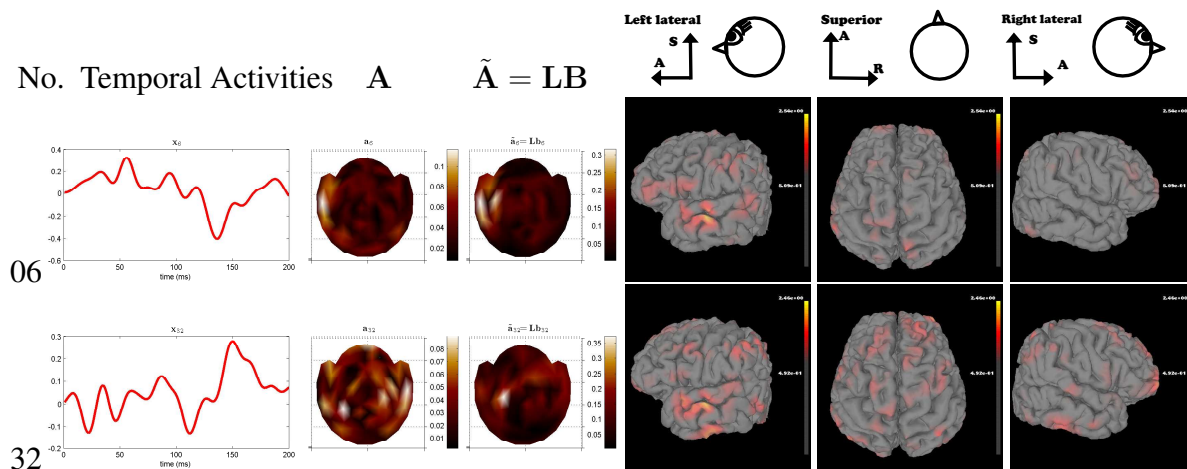


Figure 4.25: **Cortical Source Distribution of Real Data - Group 1.** Temporal activity of each component averaged out for 60 trials with duration 0 to 200 ms, topographies or said mixing matrix \mathbf{A} , reconstructed topographies $\tilde{\mathbf{A}} = \mathbf{L}\mathbf{B}$ by lead field matrix \mathbf{L} , tomographies \mathbf{B} or said the cortical source distribution shown in left-lateral, superior and right-lateral view are displayed in the order from left to right. In the first group, there are two components, numbered in 6 and 32, with strong activations in the left and right auditory area.

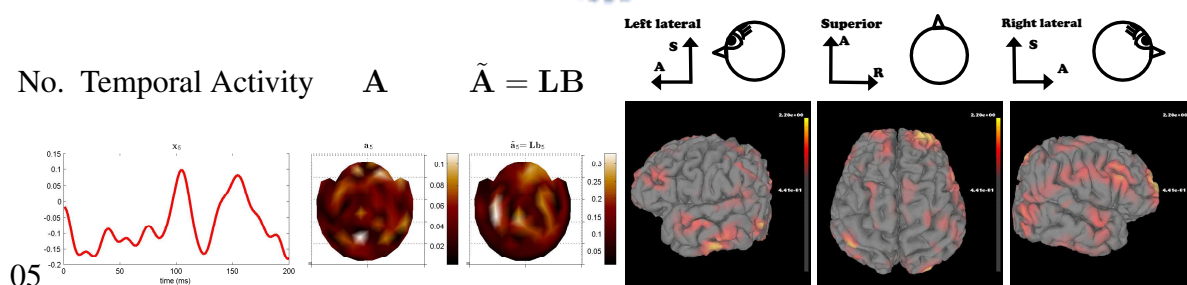


Figure 4.26: **Cortical Source Distribution of Real Data - Group 2.** Temporal activity of each component averaged out for 60 trials with duration 0 to 200 ms, topographies or said mixing matrix \mathbf{A} , reconstructed topographies $\tilde{\mathbf{A}} = \mathbf{L}\mathbf{B}$ by lead field matrix \mathbf{L} , tomographies \mathbf{B} or said the cortical source distribution shown in left-lateral, superior and right-lateral view are displayed in the order from left to right. There is only one component, numbered in 5, in the second group that is strongly activated in the right frontal cortex.

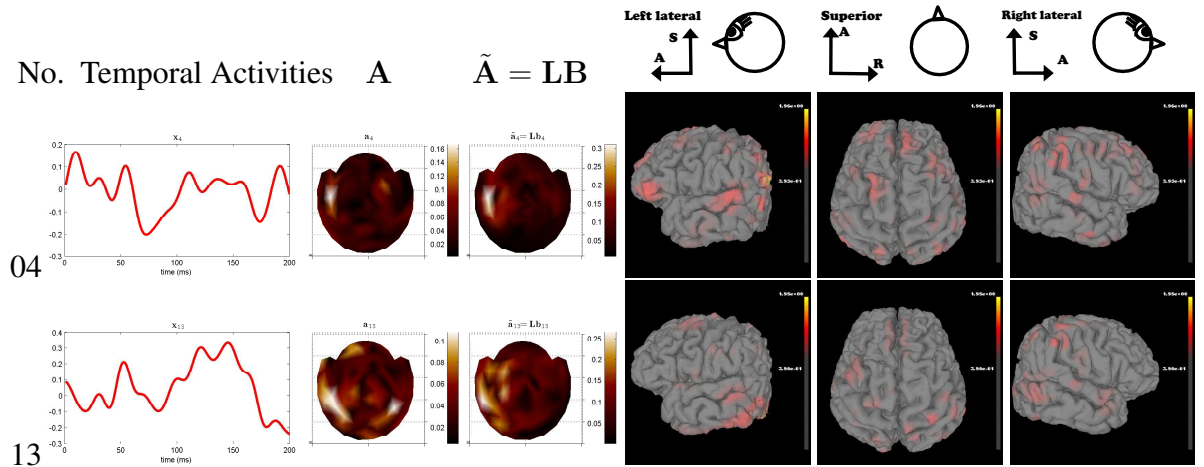


Figure 4.27: **Cortical Source Distribution of Real Data - Group 3.** Temporal activity of each component averaged out for 60 trials with duration 0 to 200 ms, topographies or said mixing matrix A , reconstructed topographies $\tilde{A} = LB$ by lead field matrix L , tomographies B or said the cortical source distribution shown in left-lateral, superior and right-lateral view are displayed in the order from left to right. There are two components, numbered in 4 and 13, in the third group with strong activations in V3 area which is part of the occipital lobe cortex.

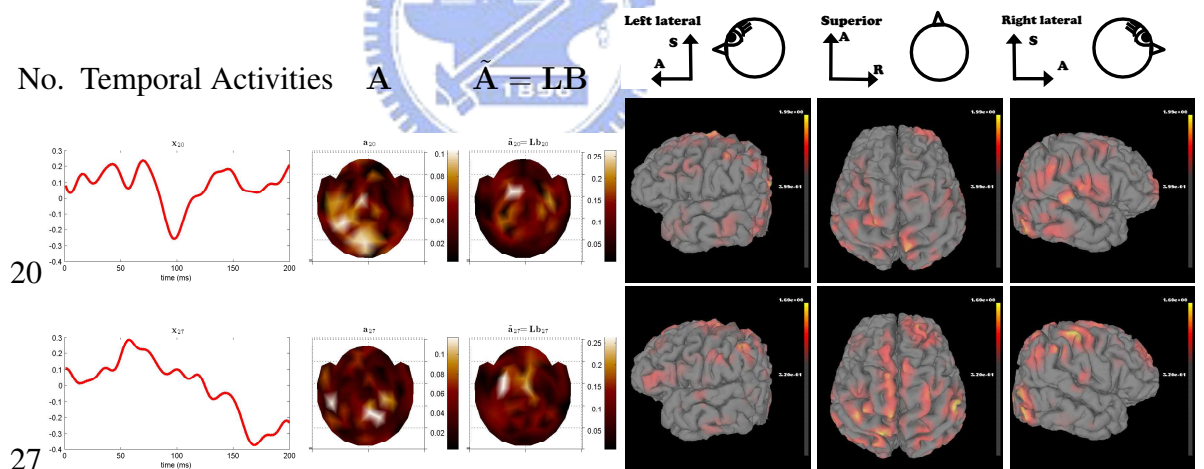


Figure 4.28: **Cortical Source Distribution of Real Data - Group 4.** Temporal activity of each component averaged out for 60 trials with duration 0 to 200 ms, topographies or said mixing matrix A , reconstructed topographies $\tilde{A} = LB$ by lead field matrix L , tomographies B or said the cortical source distribution shown in left-lateral, superior and right-lateral view are displayed in the order from left to right. There are two components, numbered in 20 and 27, in the fourth group with strong activations in both the supplementary (SMA) and primary motor cortex that played a role in planning of complex and movement coordination.

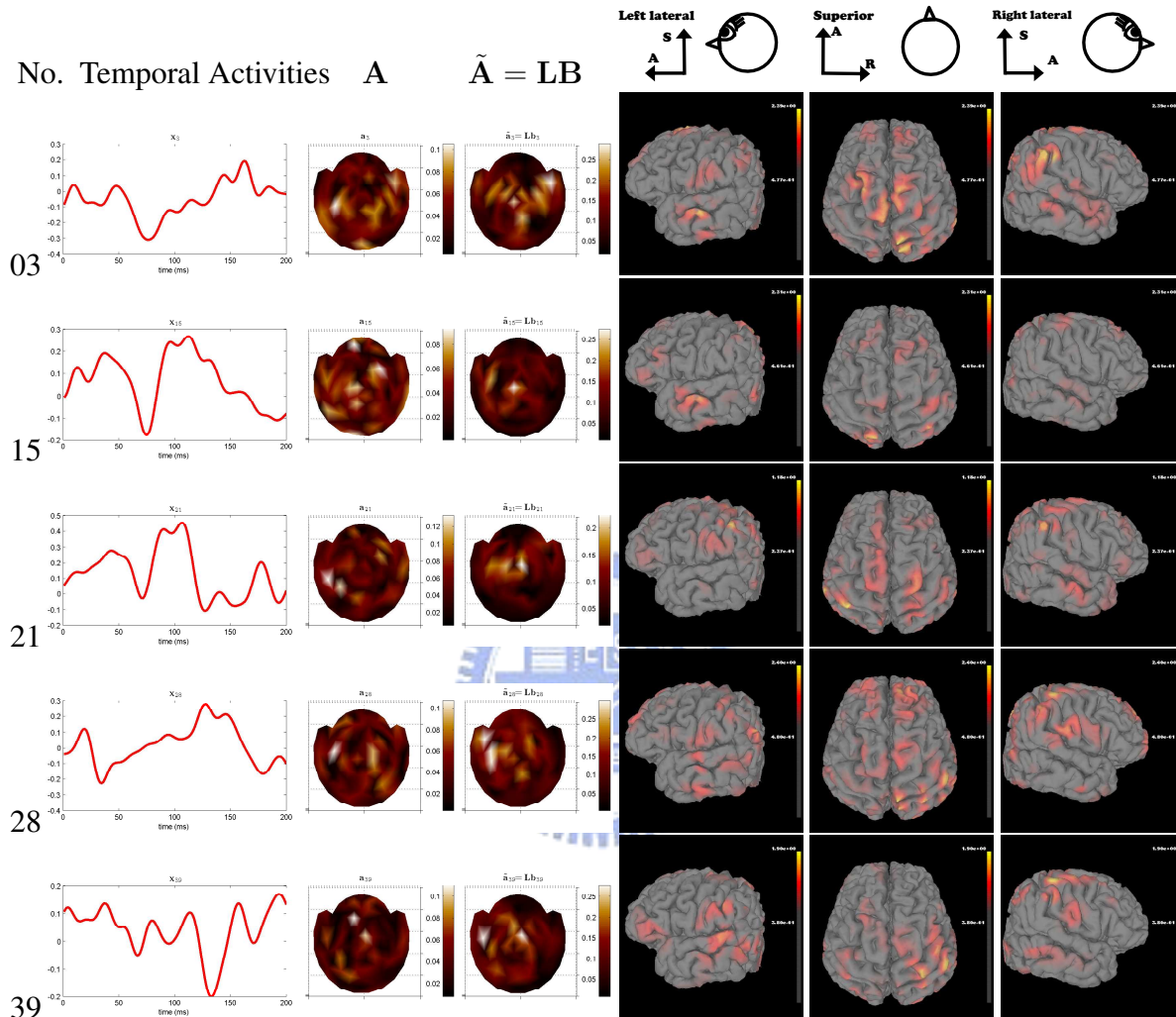


Figure 4.29: **Cortical Source Distribution of Real Data - Group 5.** Temporal activity of each component averaged out for 60 trials with duration 0 to 200 ms, topographies or said mixing matrix \mathbf{A} , reconstructed topographies $\tilde{\mathbf{A}} = \mathbf{L}\mathbf{B}$ by lead field matrix \mathbf{L} , tomographies \mathbf{B} or said the cortical source distribution shown in left-lateral, superior and right-lateral view are displayed in the order from left to right. There are five components, numbered in 3, 15, 21, 28 and 39, in the fifth group with strong activations in the primary motor cortex around the central sulcus.

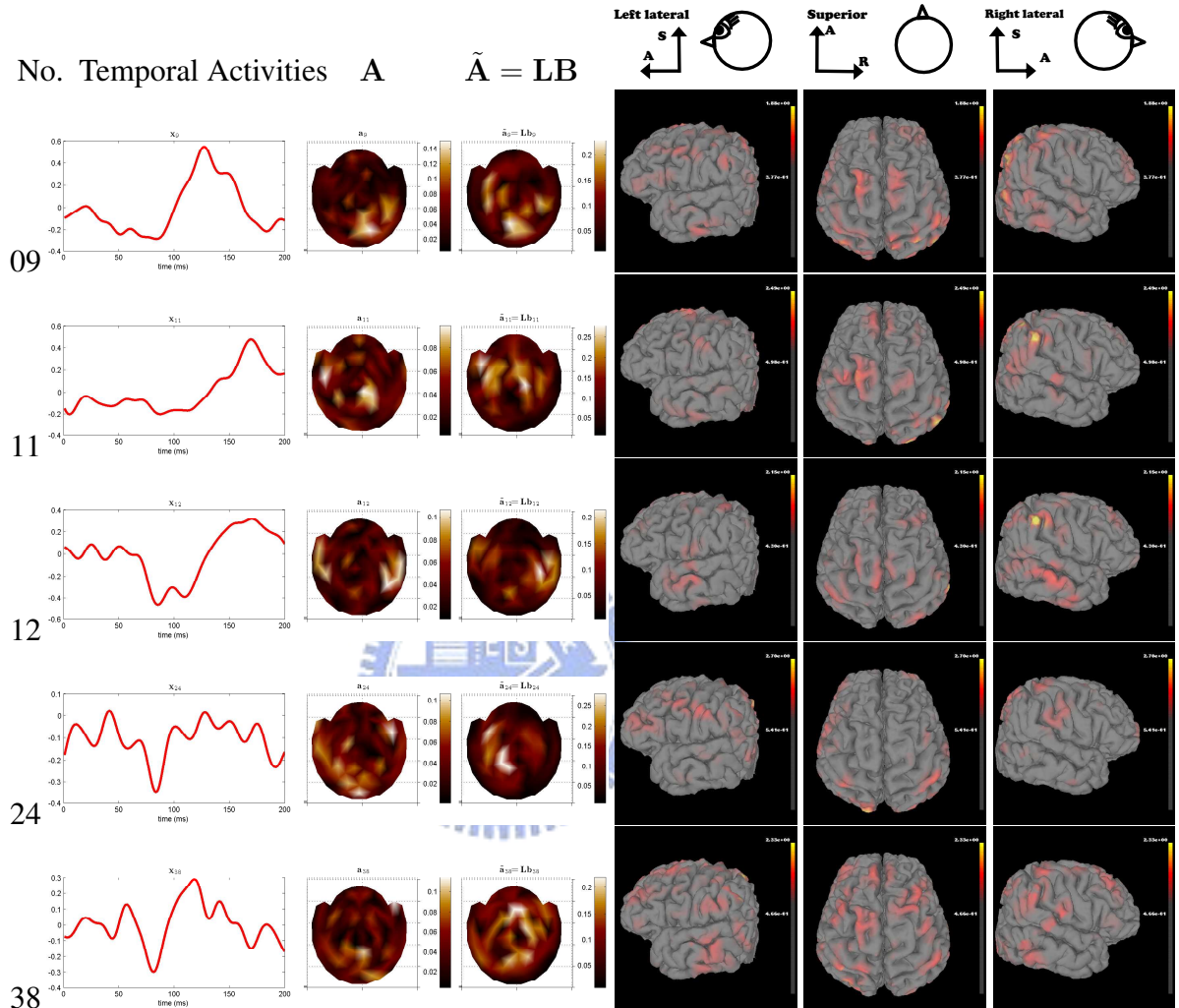


Figure 4.30: **Cortical Source Distribution of Real Data - Group 6.** Temporal activity of each component averaged out for 60 trials with duration 0 to 200 ms, topographies or said mixing matrix A , reconstructed topographies $\tilde{A} = LB$ by lead field matrix L , tomographies B or said the cortical source distribution shown in left-lateral, superior and right-lateral view are displayed in the order from left to right. There are six components, numbered in 9, 11, 12, 23, 24 and 38, strongly activated in the somatosensory cortex that believed in visuomotor coordination.

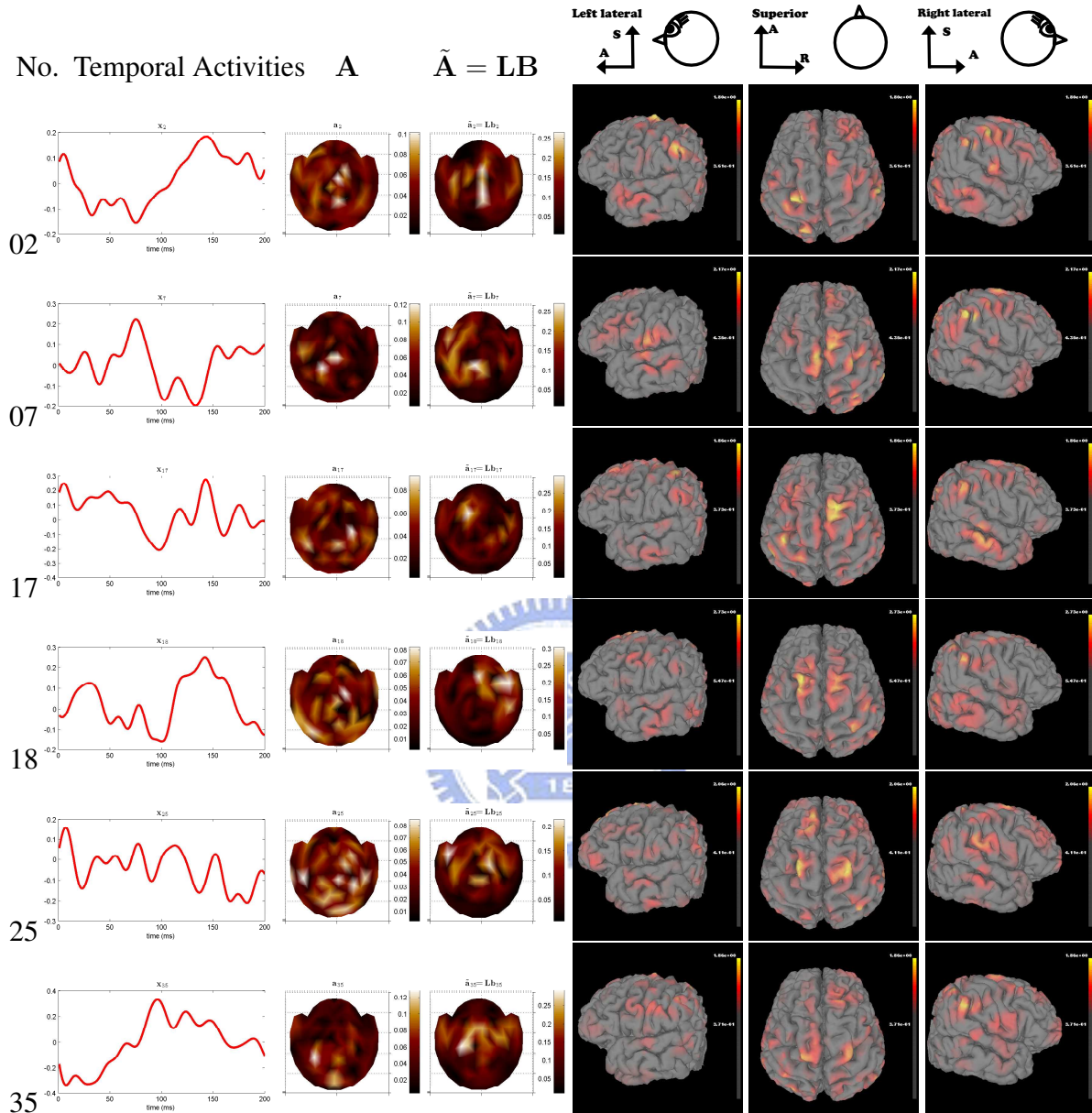


Figure 4.31: **Cortical Source Distribution of Real Data - Group 7.** Temporal activity of each component averaged out for 60 trials with duration 0 to 200 ms, topographies or said mixing matrix A , reconstructed topographies $\tilde{A} = LB$ by lead field matrix L , topographies B or said the cortical source distribution shown in left-lateral, superior and right-lateral view are displayed in the order from left to right. There are six, numbered in 2, 7, 17, 18, 25 and 35, components in the seventh group strongly activated in the somatosensory cortex that believed in visuomotor coordination.

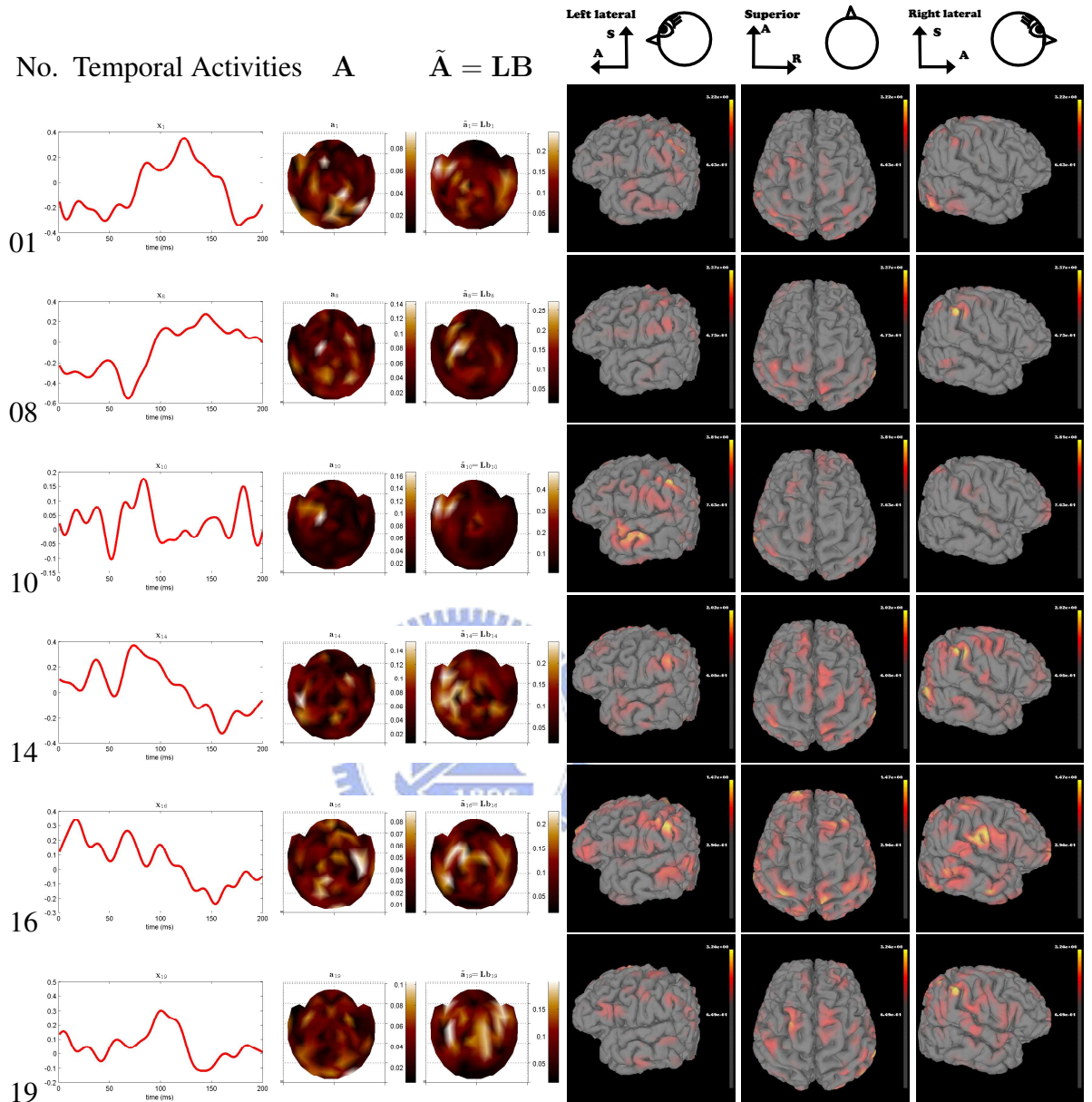


Figure 4.32: **Cortical Source Distribution of Real Data - Group 8-1.** Temporal activity of each component averaged out for 60 trials with duration 0 to 200 ms, topographies or said mixing matrix A , reconstructed topographies $\tilde{A} = LB$ by lead field matrix L , tomographies B or said the cortical source distribution shown in left-lateral, superior and right-lateral view are displayed in the order from left to right. In the last group, the eighth group, there are fourteen components with strong activations in Wernicke’s area involved in the understanding and comprehension of spoken language. The first seventh components are numbered in numbered 1, 8, 10, 14, 16 and 19. The others are shown in Figure 4.33.

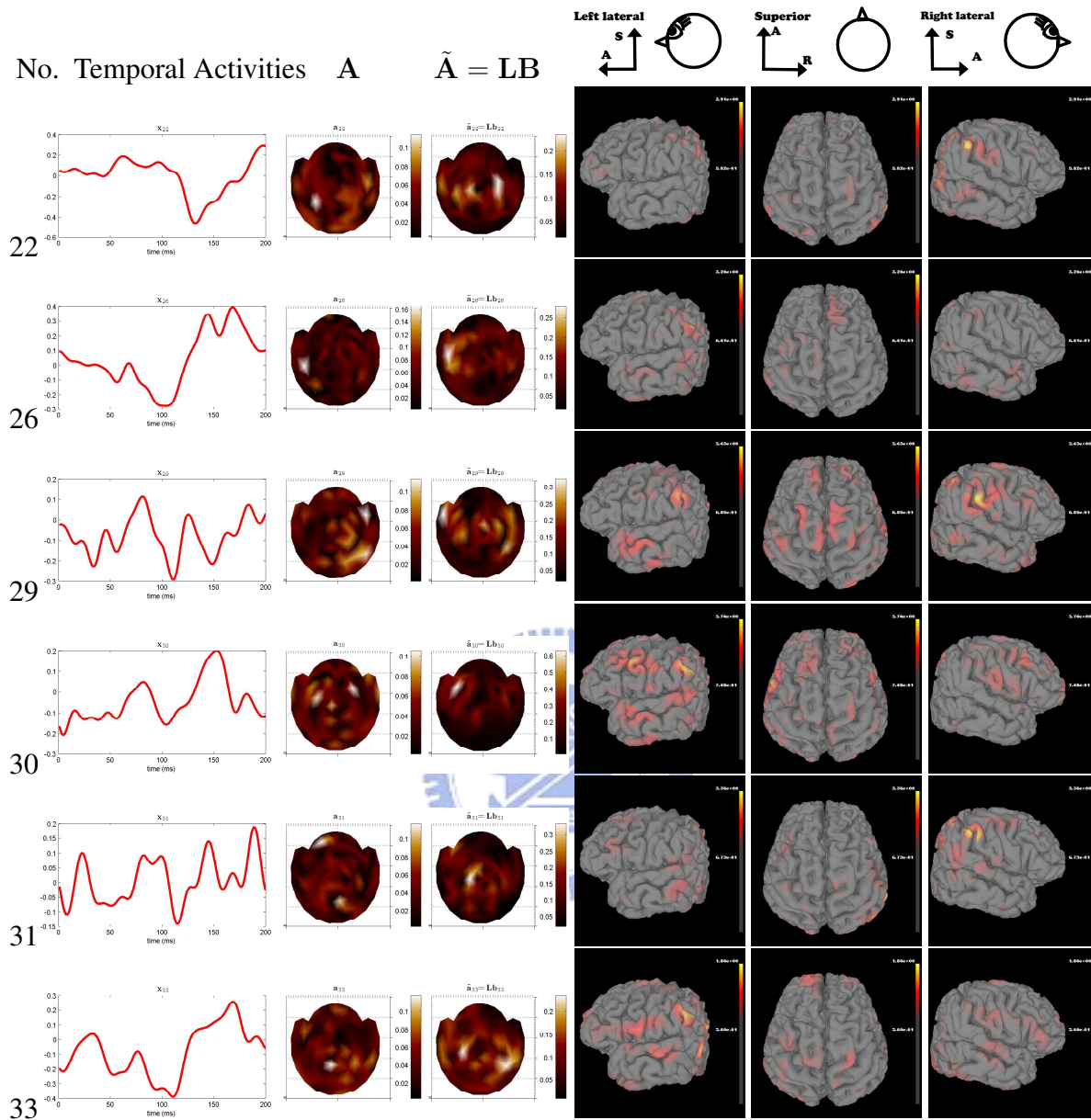


Figure 4.33: **Cortical Source Distribution of Real Data - Group 8-2.** Temporal activity of each component averaged out for 60 trials with duration 0 to 200 ms, topographies or said mixing matrix A , reconstructed topographies $\tilde{A} = LB$ by lead field matrix L , tomographies B or said the cortical source distribution shown in left-lateral, superior and right-lateral view are displayed in the order from left to right. In the last group, the eighth group, there are fourteen components with strong activations in Wernicke's area involved in the understanding and comprehension of spoken language. Another six components in the eighth group are numbered, 22, 26, 29, 30, 31 and 33. The others are shown in Figure 4.32 and 4.34.



Chapter 5

Discussion and Conclusions



5.1 Discussion

5.1.1 Accuracy and Capabilities

According to the simulations and experiment results, there is at least one source located at the same position, $(-29.47, 49.14, 94.75)$ mm, in each simulation and the tangent wave in the second simulation has the highest similarity and the least location error (Table 4.1, 4.3 and 4.5).

Although that tangent wave is not a feasible electrophysiological signal, but it can be extracted more precisely than a set of time-locked sine waves because of its independence from the surrounding random interferences, numbers in thousands, consisted of sine waves. Moreover, even in the case of the third simulation that leakage of component occurs, the method still works fine to show the reasonable cortical distribution.

Moreover, in case of a single source placed at more than one position, the cortical distribution still be rational that it indicates all the activated regions. Thus, the proposed method is both helpful and reliable since the cortical distributions of well-extracted components are agreeable to the expectation.



5.1.2 Cortical Surface Constraints

It is believed that the large pyramidal cortical neurons, numbers in tens of thousands, are the main MEG/EEG generators and their dendrites are oriented to the cortical surface. And the coherent distribution are produced by the dendrites oriented in parallel. In accordance with the spherical head model, MEG is sensitive only to the tangential component of the primary current. Thus, dipoles in sulcus are the main contributors to MEG measurements.

The spatiotemporal imaging estimated using the proposed imaging method indicates that components attempt to distribute to the adjacent sulcus aligned in parallel around the ground truth. Therefore, it is a rational explanation for the output cortical distribution of components (Figure 5.1).

In Figure fig:real-B-8-1, component No. 14 is strongly activated in the left hemisphere of brain according to the reconstructed topography $\tilde{\mathbf{A}}$ but is strongly activated in the right hemisphere of brain according to the tomography \mathbf{B} . It seems not a reasonable topography.

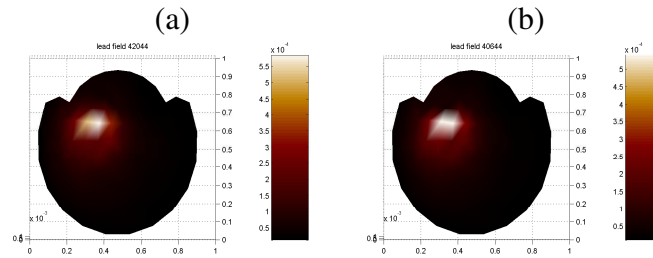


Figure 5.1: **Lead Fields of Given Source and Peak of Cortical Source Distribution of Simulation 1.** (a) Lead field of the given 15 sine of the first simulation. (b) Lead field of the peak of calculated cortical source distribution using unmixing matrix. According to the proposed method, it attempts to find a basis of lead field matrix that best represents the mixing matrix. The location error, in the first simulation, is up-to-4.67 mm because these two positions are close and with almost parallel orientations that result in similar the lead fields. Moreover, it is a rational result since brain activities are believed to be generated by a group of neighboring neurons with parallel orientation.

For observation, we plot the lead field vectors of vertices where peaks of tomography locate in the left and right hemisphere (Figure 5.2). Moreover, the norm 0.0027 of the lead field vector, with location in left hemisphere, plotted in left panel is much greater than the norm 0.0019 of the lead field vector, with location in right hemisphere. Consequently, a small value $b_{14,j}$ of tomography in left hemisphere can result in stronger effect in topography than in right hemisphere. It may explain why topography shows strong activation in left hemisphere but not in the right one.

5.1.3 Estimation With Less Parameters

One of the assumptions made by ICA is that N , the number of sensors, is greater than or equal to K , which is the number of sources [21]. In our case, N is the number of the used channels of MEG measurement and equals to 204, the number of gradiometer sensors. Besides, the cortical surface is formed by triangle mesh with P , which equals to 114,024 mentioned in Section 4.1.2, points.

Therefore, the max number of extracted independent components is 204 because ICA applying to measurement is used in sensor space. For other algorithms that decompose component in source space, the max number of independent components becomes 114,024.

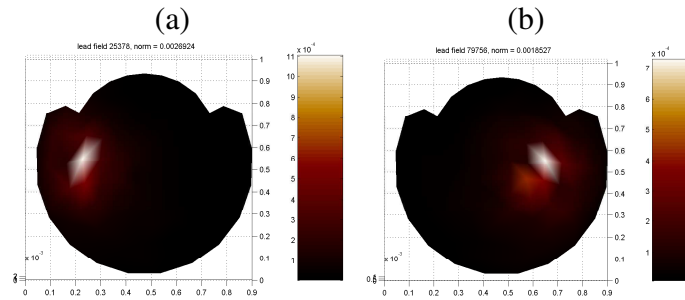


Figure 5.2: **Two Lead Fields Vectors Calculated by MCB Using Real Data.** In Figure fig:real-B-8-1, component No. 14 is strongly activated in the left hemisphere of brain according to the reconstructed topography $\tilde{\mathbf{A}}$ but is strongly activated in the right hemisphere of brain according to the tomography \mathbf{B} . It seems not a reasonable topography. For observation, we plot the lead field vectors of vertices where peaks of tomography locate in the left and right hemisphere. Moreover, the norm 0.0027 of the lead field vector, with location in left hemisphere, plotted in left panel is much greater than the norm 0.0019 of the lead field vector, with location in right hemisphere. Consequently, a small value $\mathbf{b}_{14,j}$ of tomography in left hemisphere can result in stronger effect in topography than in right hemisphere. It may explain why topography shows strong activation in left hemisphere but not in the right one.

Compare to the two kinds of algorithms, the former has the advantage of less unknown parameters, said 204, but has the limitation that no more components can be found. In contrast, the later one, such as EMSICA or beamformer-based ICA [35], has the ability to handle much more components but is difficult to have the optimal solution with too many unknown parameters, said 114,024.

5.1.4 Limitations

As mentioned above, the number of output independent components is limited to the number of used channels. Also, it is neither able to automatically pick components nor to provide the exact distribution of a badly-separated component.

5.2 Conclusions

ICA algorithms has been proposed for blind source separation. Recently, it has been proved a useful tool in neurological brain researches and is widely used for analyzing MEG/EEG signals, such as artifact removal and ERFs studying. However, one of the limitations of the standard ICA algorithms is that there is no imaging capability of it. On the other hand, there is no cortical information of the decomposed components will be obtained if applying a standard ICA to measurement. This is insufficient for studying brain activities.

We have proposed the method for imaging of independent components extracted using the standard ICA algorithms. Even though this method is neither for solving the inverse problem nor for more precisely decomposing independent component, but it has proved to be helpful and provides a both intuitive and efficient solution for mapping the discovered features or interested components of MEG/EEG signals to cortical surface. Consequently, the discovered features can be directly mapped to cortical surface without redo the experiments.

It has the advantages that simplifying the imaging problem to the small set of parameters. It has the accuracy of small location error up-to-5 mm when the components are well-separated. Besides, even a component activated at more than one place, the cortical source distribution still has been mapped well. Therefore, it is also help for study neural network that believed to be completed by the same sources. However, it is not capable to well map a badly-extracted component since it has not been separated well and corrupted by noises.

Moreover, based on the anatomical constraints, the lead field matrix for a set of data recorded by a single subject in the same time can be prepared in advanced that makes the imaging procedure easier and more efficient.

5.3 Future Works

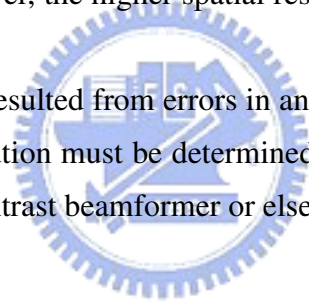
Real Data Studying

ICA is widely used for extracting features or neurological brain research in MEG/EEG. Besides, We propose this algorithm for imaging of independent components. It can be a helpful technique for finding the further explanation of the discovered features or picking new features where ignored because of insufficient informations from real data.

Cortical Constraints

It has been revealed that cortical constraint is help for improving imaging method, such as beamformer, if the co-registration and segmentation errors are smaller than 2 mm and 10° . Otherwise, even small errors in anatomical constraints can give rise to large errors in source reconstructions. Moreover, the higher spatial resolution it is, the worse effects it has [14].

Thus, to avoiding the effects resulted from errors in anatomical constraints, dipole orientations used in the forward solution must be determined on the other way, for instance, estimated using the maximum contrast beamformer or else.



Bibliography

- [1] S Baillet and L Garnero. A bayesian approach to introducing anatomo-functional priors in the eeg/meg inverse problem. *IEEE Transactions On Biomedical Engineering*, 44(5):374–385, MAY 1997.
- [2] S Baillet, JC Mosher, and RM Leahy. Electromagnetic brain mapping. *IEEE Signal Processing Magazine*, 18:14–30, 2001.
- [3] Giulia Barbati, Camillo Porcaro, Filippo Zappasodi, Paolo Maria Rossini, and Franca Tecchio. Optimization of an independent component analysis approach for artifact identification and removal in magnetoencephalographic signals. *Clinical Neurophysiology*, 115:1220–1232, May 2004.
- [4] J Cao, N Murata, S Amari, A Cichocki, and T Takeda. A robust approach to independent component analysis of signals with high-level noise measurements. *IEEE Transactions On Neural Networks*, 14(3):631–645, MAY 2003.
- [5] Yong-Sheng Chen, Chih-Yu Cheng, Jen-Chuen Hsieh, and Li-Fen Chen. Maximum contrast beamformer for electromagnetic mapping of brain activity. *IEEE Transactions On Biomedical Engineering*, 53:1765–1774, 2006.
- [6] AM Dale, AK Liu, BR Fischl, RL Buckner, JW Beldineau, JD Lewine, and E Halgren. Dynamic statistical parametric mapping: Combining fmri and meg for high-resolution imaging of cortical activity. *Neuron*, 26(1):55–67, APR 2000.
- [7] F Darvas, D Pantazis, E Kucukaltun-Yildirim, and R M Leahy. Mapping human brain

- function with meg and eeg: methods and validation. *NeuroImage*, 23 Suppl 1:S289–99, 2004.
- [8] Javier Escudero, Roberto Hornero, Daniel Abasolo, Alberto Fernandez, and Miguel Lopez-Coronado. Artifact removal in magnetoencephalogram background activity with independent component analysis. *IEEE Transactions On Biomedical Engineering*, 54(11):1965–1973, NOV 2007.
- [9] Athinoula A. Martinos Center for Biomedical Imaging. Freesurfer.
- [10] Irina F. Gorodnitsky, John S. George, and Bhaskar D. Rao. Neuromagnetic source imaging with focuss: a recursive weighted minimum norm algorithm. *Electroencephalography and Clinical Neurophysiology*, 95(4):231–251, 1995.
- [11] J Gross and A A Ioannides. Linear transformations of data space in meg. *Phys Med Biol*, 44(8):2081–2097, 1999 Aug.
- [12] M S Hamalainen and R J Ilmoniemi. Interpreting magnetic fields of the brain: minimum norm estimates. *Med Biol Eng Comput*, 32(1):35–42, 1994 Jan.
- [13] Matti Hämäläinen, Riitta Hari, Risto J. Ilmoniemi, Jukka Knuutila, and Olli V. Lounasmaa. Magnetoencephalography - theory, instrumentation, and applications to noninvasive studies of the working human brain. *Rev. Mod. Phys.*, 65(2):413–497, Apr 1993.
- [14] A Hillebrand and GR Barnes. The use of anatomical constraints with meg beamformers. *NeuroImage*, 20(4):2302–2313, DEC 2003.
- [15] Ming-Xiong Huang, Anders M Dale, Tao Song, Eric Halgren, Deborah L Harrington, Igor Podgorny, Jose M Canive, Stephen Lewis, and Roland R Lee. Vector-based spatial-temporal minimum l1-norm solution for meg. *NeuroImage*, 31(3):1025–1037, 2006 Jul 1.
- [16] AA Ioannides, E Heethaar, and K Abrahamfuchs. Point and distributed current density analysis of interictal epileptic activity recorded by magnetoencephalography. *Physiological Measurement*, 14(2):121–130, May 1993.

- [17] Tzyy-Ping Jung, Colin Humphries, Te-Won Lee, Scott Makeig, Martin J. McKeown, Vicente Iragui, and Terrence J. Sejnowski. Extended ICA removes artifacts from electroencephalographic recordings. 10, 1998.
- [18] Tzyy-Ping Jung, Scott Makeig, Colin Humphries, Te-Won Lee, Martin J. McKeown, and Vicente Iragui Terrence J. Sejnowski. Removing electroencephalographic artifacts by blind source separation. *Psychophysiological*, 37(2):163–178, 2000.
- [19] Masaki Kawakatsu. Application of ica to meg noise reduction. In *4th International Symposium of Independent Component Analysis and Blind Signal Separation (ICA2003)*, pages 535–541, Tokyo Denki University, Chiba, JAPAN, Apr 2003.
- [20] S Komssi, J Huttunen, H J Aronen, and R J Ilmoniemi. Eeg minimum-norm estimation compared with meg dipole fitting in the localization of somatosensory sources at s1. *Clin Neurophysiol*, 115(3):534–542, 2004 Mar.
- [21] TW Lee, M Girolami, AJ Bell, and TJ Sejnowski. A unifying information-theoretic framework for independent component analysis. *Computers & Mathematics With Applications*, 39(11):1–21, JUN 2000.
- [22] D. Mantini, R. Franciotti, G. L. Romani, and V. Pizzella. Improving meg source localizations: An automated method for complete artifact removal based on independent component analysis. *NeuroImage*, 40(1):160–173, MAR 1 2008.
- [23] K Matsuura and Y Okabe. Selective minimum-norm solution of the biomagnetic inverse problem. *IEEE Transactions On Biomedical Engineering*, 42(6):608–615, JUN 1995.
- [24] JE Moran, SM Bowyer, and N Tepley. Multi-resolution focuss: A source imaging technique applied to meg data. *Brain Topography*, 18(1):1–17, FAL 2005.
- [25] J C Mosher, R M Leahy, and P S Lewis. Eeg and meg: forward solutions for inverse methods. *IEEE Trans Biomed Eng*, 46(3):245–259, 1999.

- [26] JC Mosher, PS Lewis, and RM Leahy. Multiple dipole modeling and localization from spatiotemporal meg data. *IEEE Transactions On Biomedical Engineering*, 39(6):541–557, JUN 1992.
- [27] Alan V. Oppenheim, Ronald W. Schaffer, and John R. Buck. *Discrete-Time Signal Processing*. Prentice Hall, 2 edition, January 1999.
- [28] S E Robinson. Localization of event-related activity by sam(erf). *Neurol Clin Neurophysiol*, 2004:109, 2004.
- [29] S E Robinson and J Vrba. functional neuroimaging by synthetic aperture magnetometry (sam). *Recent Advances in Biomagnetism*, 1999.
- [30] S E Robinson and J Vrba. Cleaning fetal meg using a beamformer search for the optimal forward model. *Neurol Clin Neurophysiol*, 2004:73, 2004.
- [31] K Sekihara, SS Nagarajan, D Poeppel, and A Marantz. Asymptotic snr of scalar and vector minimum-variance beamformers for neuromagnetic source reconstruction. *IEEE Transactions On Biomedical Engineering*, 51(10):1726–1734, OCT 2004.
- [32] K Sekihara, M Sahani, and SS Nagarajan. Localization bias and spatial resolution of adaptive and non-adaptive spatial filters for meg source reconstruction. *NeuroImage*, 25(4):1056–1067, MAY 1 2005.
- [33] Arthur C. Tsai, Michelle Liou, Tzyy-Ping Jung, Julie A. Onton, Philip E. Cheng, Chien-Chih Huang, Jeng-Ren Duann, and Scott Makeig. Mapping single-trial eeg records on the cortical surface through a spatiotemporal modality. *NeuroImage*, 32(1):195–207, AUG 1 2006.
- [34] B.D. Van Veen and K.M. Buckley. Beamforming: a versatile approach to spatial filtering. *ASSP Magazine, IEEE*, 5(2):4–24, April 1988.
- [35] Ling-Chen Yang. Robust magnetic source imaging of brain activities. Master's thesis, National Chiao Tung University, 1001 University Road, Hsinchu, Taiwan, 300, ROC, Aug 2007.